NUREG/CR-0421
SAND78-1238
R-7

Postaccident Heat Removal: Debris-Bed Experiments D-2 and D-3

Joseph B. Rivard

Printed November 1978

Sandia Laboratories

SF 2900 Q(7-73)

Prepared for
U. S. NUCLEAR REGULATORY COMMISSION

NUREG/CR-0421
SAND78-1238
R-7

POSTACCIDENT HEAT REMOVAL: DEBRIS-BED EXPERIMENTS D-2 AND D-3

Joseph B. Rivard

Manuscript Submitted: August 1978
Date Published: November 1978

Sandia Laboratories
Albuquerque, NM 87185
operated by
Sandia Corporation
for the
U.S. Department of Energy

Prepared for
Division of Reactor Safety Research
Office of Nuclear Regulatory Research
U.S. Nuclear Regulatory Commission
Washington, DC 20555
Under Interagency Agreement DOE 40-550-75
NRD FIN No. A1181

ACKNOWLEDGMENT

A number of Sandia Laboratories' personnel made significant contributions to the D-2 and D-3 experiments. Outstanding contributors include D.N. Cox (Mechanical Design and Technical Support), D.J. Sasmor (UO_2 and Sodium), S.N. Burchett (Stress Analysis), H.G. Plein (Neutronics), A.R. Phillips (Electronic and Electrical Design and Data Analysis), D.O. Lee (Out-of-Pile Studies), I.C. Wilson and L.E. Maxey (Assembly and Testing), S.M. Falacy and C. Csinnjinni (Fabrication, Calibration, and Maintenance), the experiment operating crews, and the operating staff of the ACPR.

ABSTRACT

The second and third of the fission-heated experiments simulating fast-reactor debris in liquid sodium have been performed in the Annular Core Pulse Reactor (ACPR). These experiments were designed to assess the natural cooling capability that liquid sodium may provide for particulate debris which might be produced by a severe core-disruptive accident. Enriched UO_2 particles submersed in liquid sodium were used and were subjected to power levels ranging up to 1.28 kW/kg of oxide while the bulk sodium temperatures varied from 673 to 873 K. The particles were irregular in shape and ranged in size from about 100 to 1,000 μm. The D-2 bed loading was 600 kg/m^2 of oxide and the D-3 loading was 900 kg/m^2.

Dryout (expulsion of liquid by vapor generation) of the lower part of the beds occurred in D-2 and D-3 at power levels of 0.76 and 0.40 kW/kg of oxide, respectively. Rather than leading to high temperatures, the dryout temperature transient led to the attainment of near-equilibrium temperatures in the dryout zone which were only modestly higher than pre-dryout levels. Analysis provides a formula for the occurrence of dryout and proves that the observed temperature signal is primarily due to dryout zone expansion. It is concluded that the main result of dryout is the shortening of convection flow paths and, while dryout may be necessary for the attainment of temperatures which could threaten reactor containment, it may not be sufficient for that to occur.

CONTENTS

ILLUSTRATIONS

ILLUSTRATIONS (cont)

TABLES

NOMENCLATURE

A	=	constant in settling equation; constant in Z equation
B	=	constant in Z equation
C_ℓ	=	specific heat of liquid
c	=	bed loading; specific heat
D	=	diameter
F	=	general function
g	=	gravitational constant
k	=	thermal conductivity
k_B	=	effective bed conductivity
K	=	empirical constant for irregular particles
L	=	bed height
L^*	=	reduced bed height; effective convection length
(L^*)	=	modified reduced height
$\mathscr{L}$	=	heat vaporization
N_u	=	Nusselt number
p	=	power per unit mass
q	=	volumetric heat generation rate
R_{a_1}	=	single-phase Rayleigh number
r	=	percent of operating power
s	=	specific gravity
T_B, T_C	=	temperature (bottom, top)
t	=	time
v	=	velocity
V_T	=	terminal velocity
x	=	distance
X	=	general variable
z	=	coordinate in dryout zone
Z	=	thickness of dryout zone
α	=	thermal diffusivity
β	=	constant in Z equation
γ	=	constant in Z equation
$\Delta\rho$	=	density difference
ΔT_s	=	subcooling

NOMENCLATURE (cont)

ϵ	=	porosity (sodium volume fraction)
η	=	viscosity
θ	=	temperature elevation above sodium saturation
κ	=	permeability
λ_n	=	nth parameter
ρ	=	density of solid
ρ_L, ρ_ℓ	=	density of liquid
ν_v, ν_1	=	kinematic viscosity of vapor, liquid
ξ	=	nonequilibrium measure

POSTACCIDENT HEAT REMOVAL: DEBRIS-BED EXPERIMENTS D-2 and D-3

Introduction

In the unlikely event of a severe accident in a sodium-cooled fast reactor, molten core materials may contact liquid sodium, resulting in rapid quenching, freezing, and fragmentation of the core debris. This debris may settle on available surfaces within the reactor vessel, forming debris beds. Assuming no recriticality occurs, the fuel in these debris beds will be heated only by the radioactive decay of retained fission products and actinides. If the debris beds are submerged, the liquid sodium surrounding the particles will afford some cooling. However, if this cooling is not adequate, the particles of fuel may increase in temperature and eventually remelt, causing failure of internal structure and threatening the reactor vessel itself.

If the reactor vessel is attacked by molten fuel, a breach would allow molten fuel, molten steel, and liquid sodium to flow into the lower portions of the containment structure, where they could further interact. Again, debris beds, consisting of fuel and steel particles submerged in sodium, might be formed and might threaten the containment.

The hazard level to be assigned to these severe postaccident scenarios obviously depends upon the extent to which natural cooling of the debris may be relied upon. The need for studies of phenomena following debris-bed remelt depends to a large extent upon how effectively the bed is cooled. A computer-based model of the postaccident scenario is currently being developed.[1] Its purpose is the analysis of the response of advanced reactor-containment systems to a core disruptive accident (including core meltdown), beginning with the breach of the reactor vessel and following the postaccident sequence through the breach of the secondary containment.

The experiments described herein have as their basic purpose the investigation of the cooling of debris beds, including an assessment of the likelihood of fuel remelting and subsequent damage to the reactor vessel. Prior to performance of the D-1 experiment[2], experiments on debris-bed behavior either used substitute materials (e.g., sand and water) or employed real reactor materials, but atypical heating methods. In order to adequately simulate decay-heated debris, it is necessary to generate heat within the oxide fuel material. In the D-series of experiments, this is accomplished by steady-state fission heating of U-235-enriched UO_2 particles submerged in liquid sodium. The experiments are carried out in the central irradiation cavity of the Annular Core Pulse Reactor (ACPR), located at Sandia Laboratories, Albuquerque, NM.

In the reactor situation being simulated, the debris would tend to be partly cooled on its bottom by thermal conduction through the structure supporting it. Also, for a finite bed, additional cooling would occur at the sides of the bed. However, in the initial D-series experiments, conservative results have been sought by employing insulated boundaries on the bottom and sides of the bed, thus increasing the likelihood of overheating.

This report describes the conduct and results for the D-2 and D-3 experiments which followed the D-1 experiment. Preliminary information on these experiments was published earlier.[3,4]

Due to the similarity of the D-series experiments, much of the background material on the experiments applies to all of them. Because this information is contained in Reference 2, it is not repeated here. Included in Reference 2 is a description of the experiment package, the helium cooling system, supporting experiments and analysis, and the general experiment procedure.

This report contains a description of the pertinent details of the D-2 and D-3 experiments under "Experiment Description," followed by descriptions of the conduct of the experiments and what was observed during them. Next, the section titled "Analysis and Interpretation of Results" describes the analysis which was applied to the data collected during the two experiments and offers interpretations of the results. This is followed by the "Summary and Conclusions."

Decay-Heat Source Term

The heat-source term of interest for postaccident heat removal (PAHR) is produced by decay of the fission products and actinides resulting from power operation of the reactor. It should be noted that this source cannot generally be stated with precision due to its dependence upon the operating history of the reactor and because of error and scatter in measurements and calculations of the decay. In addition, the fraction of the source which appears as heat within the fuel debris depends upon two basic factors: escape of fission products from the fuel matrix and escape of gamma rays. The latter factor has been treated previously;[2] the former factor is dependent upon a host of conditions, most of which cannot be accurately specified in advance. (Turland and Peckover[5] have recently provided a review of fast-reactor decay-heat topics.) Since debris is formed from fuel that has previously been molten, it is reasonable to assume that the volatile and gaseous species are no longer present in the debris. Thus, the ensemble of all decaying fission products and actinides constitutes a most conservative (larger than actual) upper bound on the heat source within a debris bed.

Recently, Murley et al[6] compared data and analysis on thermal-reactor fission product decay heat with the ANS Standard (1971).[7] If a 20% allowance for decay of actinides is added to this data, a conservative decay-heat source term may be specified (no allowance for continuing fission is included, however). From one second to several hundred seconds after neutronic shutdown, this specified source term is closely approximated by $r = 7.3 - 0.8034 \ln(t)$, where r is percent of operating power and t is time after shutdown in seconds. (Part of this curve is shown in Figure 1.) If it is assumed that a debris bed is fully formed 1 s after neutronic shutdown

(very rapid formation), then this formula may be used to compute the rise rate of the debris temperature above the bulk temperature of the sodium. This has been done for a debris bed with a 0.43 volume fraction of sodium; the result is shown in Figure 1. (It was assumed, for the purpose of this calculation, that the initial temperature was 773 K (500°C), that no heat was lost from the bed, and that sodium was removed from the bed at the sodium boiling point, without vaporization.)

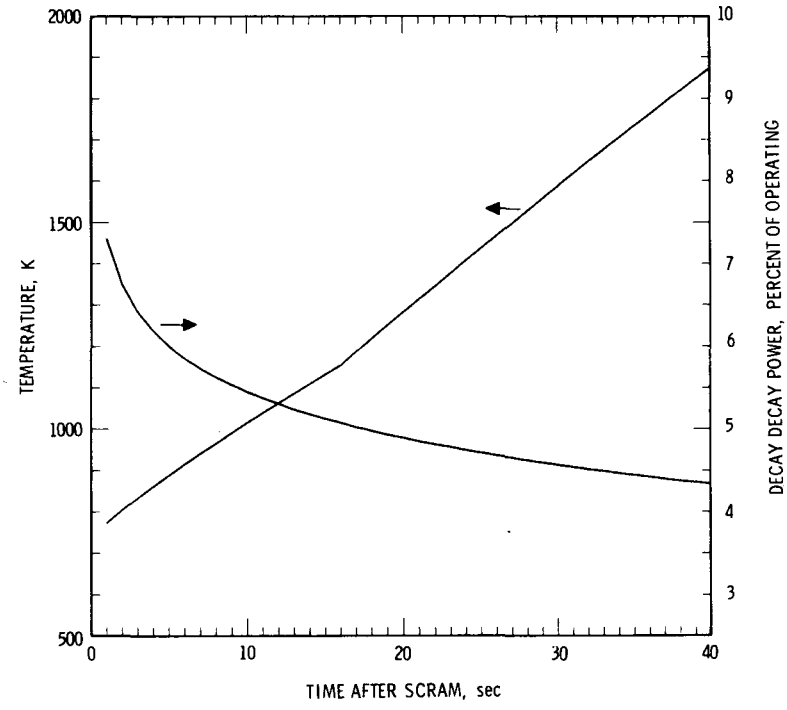

Figure 1. Decay heat (right-hand legend) as given by r = 7.3 - 0.8034 ln (t), where r is percent operating power and t is time in seconds after neutronic shutdown. Debris bed temperature rise (left-hand legend) is given for a bed formed 1 s after shutdown.

This calculation shows that, even with these very conservative assumptions, local sodium boiling within the bed could not commence until 16 s after shutdown (break in curve denotes boiling point). At this time, the source term is reduced to about 5%. According to these calculations, the melting temperature of steel could not be reached until after more than 33 s; at this time, the source term is reduced to about 4.5%. UO_2 melting could not commence until after more than 88 s, when the source is reduced to near 3.7%. Since a typical fast-reactor power level (averaged over the whole core) is roughly 100 kW/kg of oxide, it can be seen that 5 kW/kg of oxide is a very conservative value of the maximum power required to simulate a debris bed.

Differentiation of the percent formula gives the rate of decrease of the power level. At 1 s after shutdown, the decay power is decreasing at nearly 1%/s (about 1 kW/kg). At +20 s, power is decreasing 2.4%/min, and at +100 s, power is decreasing at a rate of about 0.5%/min

(0.5 kW/kg). The rapid decrease of power during the early time after neutronic shutdown illustrates the conservatism inherent in steady-state power simulations, and points up the fact that phenomena which develop slowly during steady-state power simulations may not develop completely or may not develop at all when the heating is radioactive decay.

Effect of Bulk Sodium Temperature

In the usual Loss-of-Flow (LOF) or Transient-Overpower (TOP) accident scenario, the core-disruptive accident is assumed to occur in the presence of otherwise-normal operating circumstances. Thus the starting bulk-sodium temperature of interest for postaccident heat removal is very nearly the operating bulk temperature. For a typical fast reactor, the bulk temperature is usually about 400 K below saturation. The D-series experiments and analysis described in this report are applicable to this subcooled bulk condition.

Analysis by Kazimi et al,[8] of the postaccident situation in the Clinch River reactor following complete loss of pumping power, with successful scram and a totally plugged core, indicates that natural convection within the primary loop, driven by decay heating in the core region, will produce sodium flow rates ranging from 1 to 2% of operating flow rates. Thus, for 673 K (400°C) inlet temperatures, outlet temperatures from 773 K (500°C) to 1023 K (750°C) are calculated. According to the authors, an inlet temperature of about 1023 K (750°C) would be needed, at 1% decay power, to boil sodium in the upper plenum.

The Kazimi et al analysis assumes that heat continues to be removed from the primary system following a LOF or TOP, and finds that the bulk sodium remains substantially subcooled. In the so-called Loss-of-Heat-Sink (LOHS) accident sequences, however, different results are obtained. In these alternate accident scenarios, the initiating event is loss of all heat-removal systems, accompanied (or caused in some cases) by primary pipe ruptures which allow escape of sodium. Successful scram of the reactor is assumed, so that gradual heatup of fuel is caused by the decay-heat source. The analysis of Chan et al[9] assumes that the accident sequence is initiated by a sudden rupture of primary piping (as might be caused by a violent earthquake), leading to a prompt lowering of sodium level to that of the break. Natural circulation within the reactor vessel, between lower and upper plena, removes heat from the core to the bulk of remaining sodium. Subcooled boiling in the core, followed by bulk boiling, leads to recession of the sodium level. This is followed by clad melting and failure of fuel subassemblies, leading to the potential for recriticality.

The analyses of Bari et al,[10,11] on the other hand, assume failure of all heat removal capability as an initial condition, including natural convection in the primary loop, although natural convection within the reactor vessel was assumed where appropriate. In some cases, primary piping rupture was also assumed. Core meltdown occurs due either to dryout in the boiling region of the core or to uncovering of the core by recession of the sodium level. Potential recriticalities are assessed.

From the standpoint of postaccident heat removal, the LOHS scenarios are important in that they lead to conditions in which debris may be submersed in sodium which is at, or near, its saturation temperature, and to which the D-series experiments described herein are not directly applicable.

Much of the debris-bed experimentation reported previously has utilized coolants which are at, or near, their saturation temperatures. The resulting phenomenological models of boiling-bed behavior follow the vapor-channel model proposed by Gabor et al[12] in which the packed-bed depth of the debris is reduced by the formation of vapor-exit channels in the upper parts of the bed. These vapor channels are formed in coolants near saturation temperature by the force of vapor exiting the upper surface of the bed. It seems clear that such vapor forces will be much reduced (or not exist at all) in beds submerged in substantially subcooled liquid, due to vapor condensation before it reaches the upper surface. Therefore, the model discussed below, based upon the D-series experiments in subcooled sodium, does not incorporate vapor channels and may not, therefore, be applicable to beds in saturated sodium.

The final matter to be emphasized here is that, due to the large amount of sodium contained in fast reactors of interest, the rise in bulk temperature to the saturation level consumes, in the LOHS scenarios, something in excess of 10^4 s beyond the time of successful scram. At these late times, decay power has decreased to levels of 1% or less. This substantially reduces the potential cooling problem for decay-heated debris.

The Influence of Settling

In the scenario following a core disruptive accident, it is assumed that molten fuel is injected into regions filled with liquid sodium. Quenching of the hot fuel by the relatively cool sodium causes the fuel material to refreeze and shatter into solid particulate material, which subsequently settles onto obstructing surfaces forming so-called debris beds.

It is well known that the manner in which a bed of particles is formed strongly affects the permeability of the bed. This effect is also presumed to hold for a bed of debris formed by particles settling out from liquid sodium. Since the permeability of a debris bed will influence its natural cooling capability, it is of interest to examine the influence which settling may have on the structure of the bed.

A scoping calculation of the settling influence may be performed in the following way. Assume that the particles may be represented by discrete groups having nominal "diameters" (D) of 100, 500, 800, 900, and 1000 μm. Assume that each of these particle groups falls from rest through a liquid with a viscosity (η) for a distance (x). Initially, each particle must accelerate from rest. Depending on the size of the particle and if x is large enough, the particle velocity will attain its limiting or "terminal" value and will continue to fall at this velocity until stopped by an obstruction. The largest particles will impact the obstruction in the shortest time. Therefore, the height of each particle-size group at the time of impact of the 1000-μm group is a measure of the "spread" between particle sizes which will occur during settling.

Assuming low Reynolds numbers, a particle acted upon by viscous drag alone will accelerate from rest with a velocity

$$v = V_T \left(1 - e^{-18\,\eta t/\Delta\rho D^2}\right) \quad .$$

where t is time, $\Delta\rho$ is the density of the solid minus the density of the liquid, and V_T is the terminal velocity which may be taken to be

$$V_T = Ks^{2/3}D/\left(\rho_L \eta\right)^{1/3} \quad ,$$

where s is the specific gravity of the particles, ρ_L is the density of the liquid, and K is an empirical constant determined for irregular particles.

Integrating and solving for the distance x(D,t) traveled by a particle of diameter (D) in a time (t) yields an equation of the form

$$x(D,t) = V_T\,(D)\left[t - A(D)\left(1 - e^{-t/A(D)}\right)\right] \quad .$$

where A(D) is a constant for a given-sized particle. Distances computed from this formula may be arranged as shown in Figure 2, with the "spread" of the particles at the time of impact of the 1000-μm-size group plotted versus the settling distance (or height).

Although the above simplified analysis does not account for complicated effects such as particle-particle interaction and wake influence, it nevertheless infers certain trends. The "spread", and thus the tendency for size separation in the bed (with larger particles on the bottom and smaller particles on the top), increases substantially as the settling distance is increased. The smallest particles ($\leq$ 100 μm) will probably always settle out on the top of the bed, regardless of the settling distance. When the settling distance is several meters, reasonably good size separation of all particles should occur.

The implication which these trends have for the natural cooling capability of debris beds is most easily seen in a comparison with a uniformly mixed bed. As a consequence of the lack of smaller particles near its bottom, the settled bed will possess a permeability which increases with depth, in contrast to the uniform permeability of the uniformly mixed bed. (The bed porosity will also be greater toward the bottom.) In addition, the permeability in the lower regions of the bed should substantially exceed that of the uniformly mixed bed of similar-sized particles, especially for larger settling distances. Because permeability characterizes the ease with which a fluid may flow through the porous medium by an applied pressure gradient, it is clear that convection should be a more predominant mode of heat transport in the lower regions of settled

beds. Because the lower regions of beds tend to operate at higher temperatures, the enhanced convection capability should flatten the temperature profile by reducing the maximum temperature attained within the bed for a given power level, thus increasing the natural cooling capability.

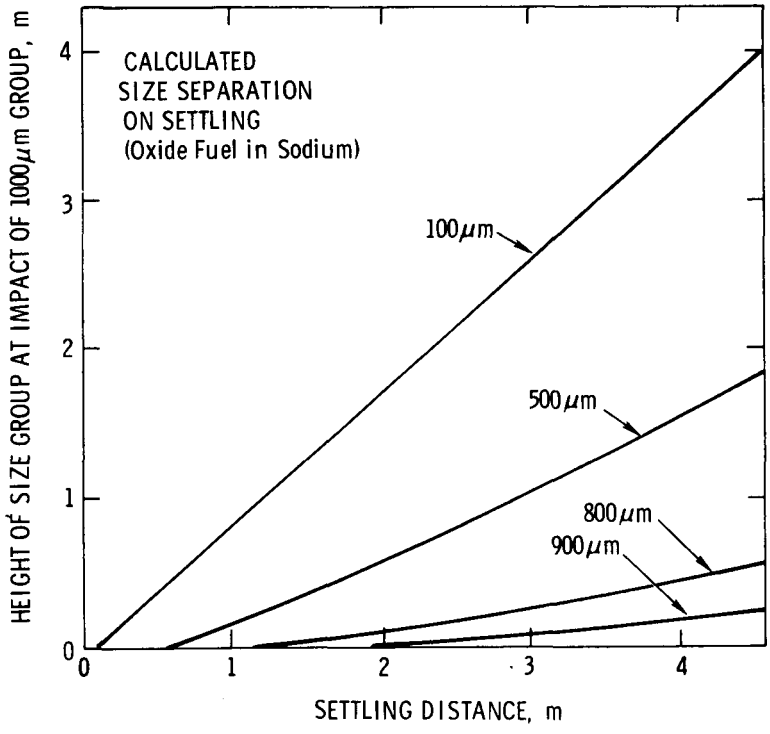

Figure 2. Calculated Size Separation on Settling (oxide fuel in sodium)

Key Issues

A number of key issues must be resolved to facilitate understanding of postaccident heat-removal processes from debris beds. This understanding will further the safety assessment required for the licensing and operation of advanced fast reactors for electric power generation. These issues include:

a. Is debris-bed cooling strongly influenced by bed depth?

b. How does the subcooling of the bulk sodium affect debris-bed cooling?

c. Will the agitation of sodium boiling tend to level debris beds with varying depths?

d. Will dryout (liquid expulsion by vapor generation) occur in debris beds?

e. Will debris-bed dryout lead to remelting of the fuel?

f. What is the nature of debris-bed heat transfer?

g. Can out-of-pile experiments be used to predict debris-bed behavior?

h. What is the role of the bed formation process in debris-bed behavior?

The experiments described herein are part of a program designed to investigate and elucidate these issues.

Experiment Description

In these experiments, a quantity of fully-enriched UO_2 particles of irregular shape and with a size distribution ranging from 100 to 1000 μm (Figure 3) is fission heated within the irradiation cavity of the ACPR to simulate decay heating of fuel debris. In each experiment the UO_2 particles are contained in a closed, flat-bottomed vessel of 102-mm inside diameter which is insulated on the lower diameter and bottom (Figure 4). Sufficient sodium is included inside of this vessel to saturate the particle bed and to provide a volume of bulk sodium above the bed. This bulk volume of sodium is maintained at a constant selected temperature by a helium cooling system[13] which supplies a controlled flow of helium to an external helical heat exchanger surrounding the upper part of the vessel. At the top of the vessel, the volume above the sodium liquid contains helium at low pressure (35 kPa @ 473 K). This volume also houses two pressure transducers. It allows for volumetric expansion of the liquid sodium.

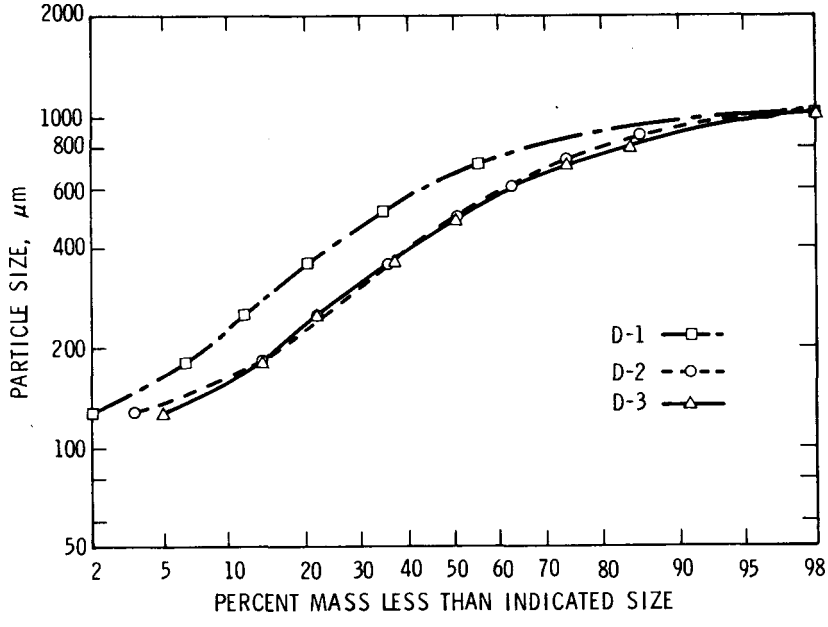

Figure 3. Particle-Size Distributions for the D-Series Experiments

Type-K thermocouples are located in the particle bed and in the liquid sodium. Figure 5 shows the location and designation of the thermocouples in the bed. The thermocouples are sheathed with Inconel; both grounded junctions and ungrounded junctions have been employed.

A more detailed description of the apparatus and instrumentation it given in Reference 2.

Table I gives values of several parameters for the D-1, D-2, and D-3 experiments.

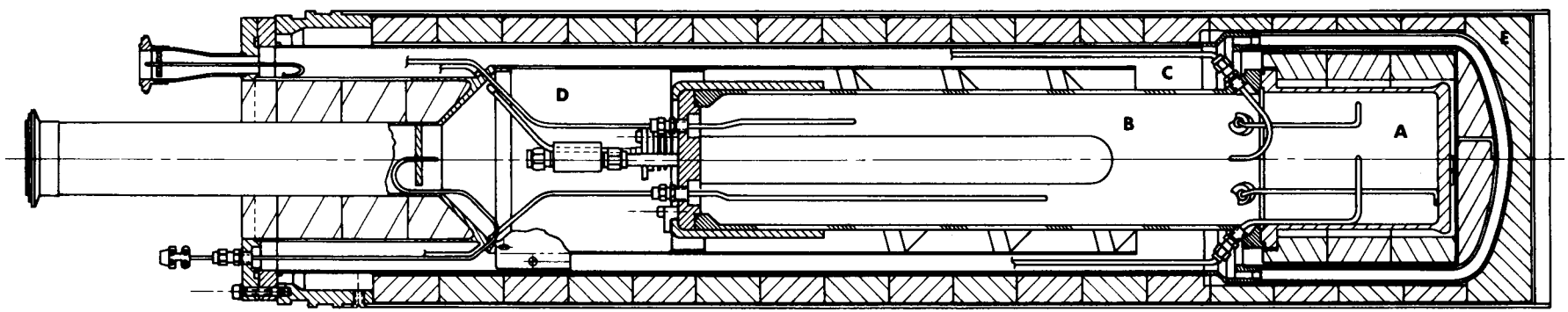

Figure 4. Debris-bed experiment capsule, showing A, location of bed in containment vessel with liquid sodium at B; C, entrance for helium coolant to helical upflow heat exchanger; D, exit plenum for hot helium; E, typical solid insulation.

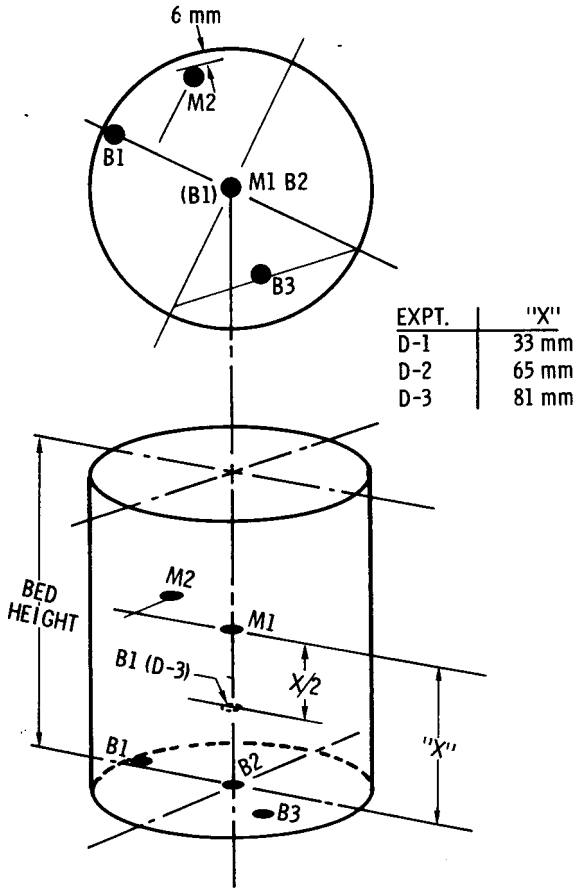

Figure 5

Location and Designation of Thermocouples in the D-Series Experiments

TABLE I

Debris-Bed Experiment Parameters

Parameter	D-1	D-2	D-3
Bed Loading (UO_2) kg/m^2	300.	600.	899.
Total Fuel (UO_2) kg	2.432	4.866	7.292
Bed Depth, mm	58.	106.* (99.-113.)	158.
Max. Specific Power (UO_2) kW/kg	1.0	1.28	0.43
Sodium Mass, kg	2.837	2.924	3.131
Gas Volume @ 473 K, m^3	0.98 (10^{-3})	1.00 (10^{-3})	1.07 (10^{-3})
Sodium Volume Fraction in Bed	0.48	0.43	0.43
Bulk Sodium Temperatures, K	673, 773, 823, 838	673, 873	673, 773, 873
Max. Observed Temperature, K	1007.	1188.	1265.

*Average value, bed surface inclined

In the second experiment in the series, D-2, 4.87 kg of UO_2 formed a bed with an average depth of 106 mm. The surface of the bed was actually slightly inclined to the horizontal (Figures 6 and 7), with measurements showing the extremes of depth to be 99 mm and 113 mm. The average porosity (sodium volume fraction) within the bed was 0.43. The bed was fission heated for more than 30 hours during the experiment.

In the D-3 experiment, 7.29 kg of fully enriched UO_2 formed a bed about 158 mm deep. The average porosity within the bed was 0.43. The bed was fission heated for nearly 30 hours during the experiment. Figures 8 and 9 show X-rays of the experiment taken prior to the start of experiment operation.

During each experiment, the mode of operation is as follows: With the sodium melted and the ACPR at a very low power level, a bulk sodium temperature level is established by adjusting the setpoint input to the automatic temperature control of the helium cooling system. When the steady-bulk sodium temperature has been achieved, the ACPR power is incremented upward to a higher level. Within approximately 20 minutes, system thermal transients have died out and steady readings are taken. Usually, readings are taken also at 40 minutes prior to again incrementing reactor power upward. After the power level has attained the reactor's maximum, the power is reduced to a low level and a new bulk-sodium temperature is established. Upward power incrementation is then begun again.

Because of the potential hazard of the experiments, safety precautions govern all aspects of experiment operation. Assurance of containment is maintained by a limit on the temperature of the bottom of the debris-bed vessel and radiological monitoring. Stipulated procedures govern the safe reduction of reactor power to 10 kW for the termination of a dryout transient. No safety or radiological incident occurred during any of the experiments.

D-2 Experiment

During the D-2 experiments, specific power levels of up to 1.28 kW/kg of UO_2 were achieved. Three heating cycles at temperatures of 673, 873, and 673 K (400, 600, and 400°C) were performed to study the effect of sodium subcooling. The specific power of 1.28 kW/kg corresponds to the maximum reactor power permitted (600 kW). In general, temperatures within the bed were laterally uniform, although the midheight thermocouples (M1 and M2 in Figure 5) registered differences of up to 50 K early in the experiment as power was incremented upward at bulk temperatures of 673 K and less.

As power was incremented upward at 673 K during the first heating cycle, the bed behavior initially resembled the thermal-conduction mode observed during the D-1 experiment.[2] (The calculated single-phase Rayleigh numbers are less than 15.) During this cycle the ACPR power level was being incremented in steps corresponding to 0.04 kW/kg. At approximately 0.5 kW/kg, boiling was observed to occur at the bottom of the bed at 1131 K (858°C) (all three thermocouples) while the upper part of the bed continued in the conduction mode up to a power level of 0.76 kW/kg.

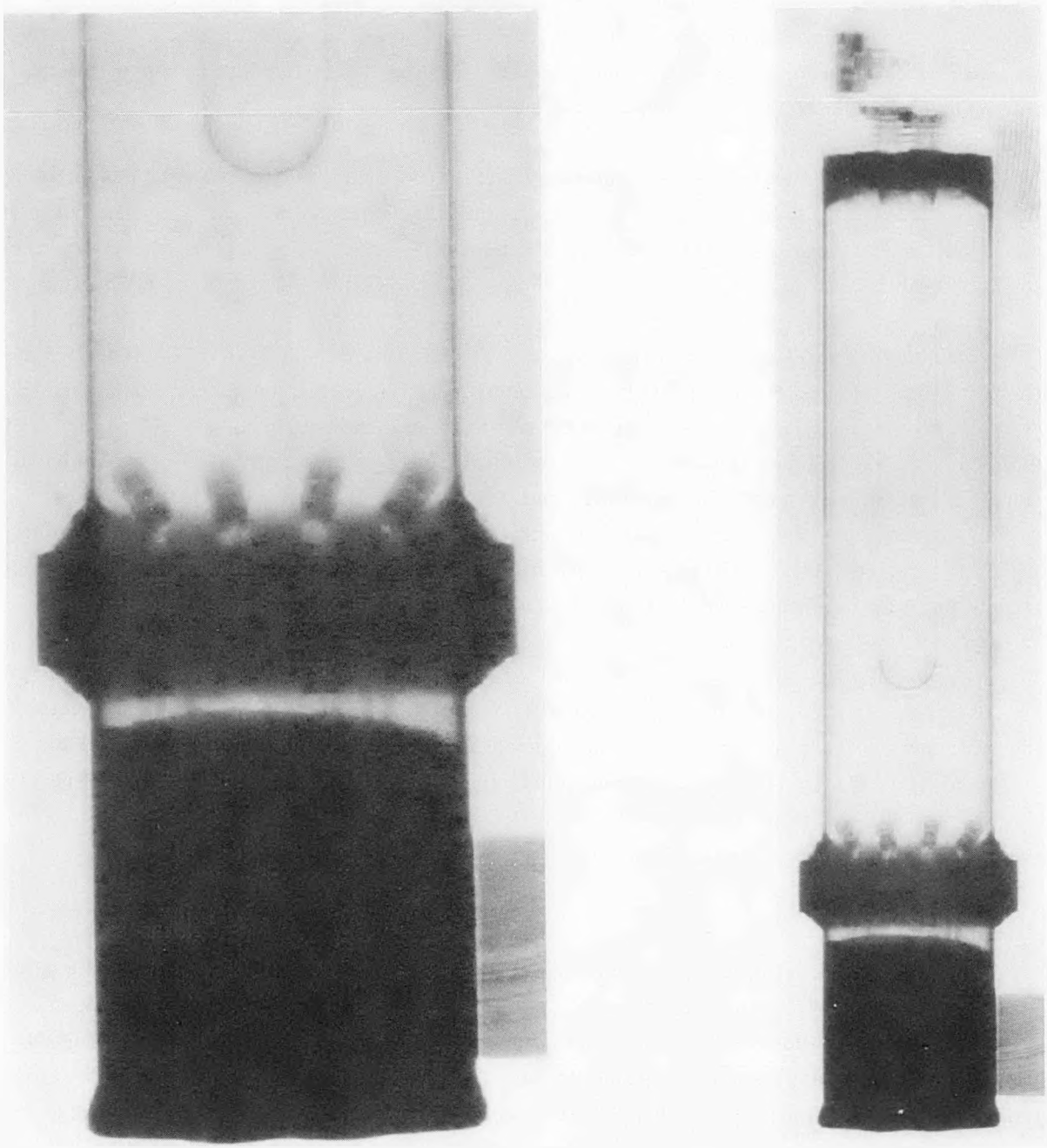

Figure 6. X-Ray of D-2 Containment Vessel After Filling. The frozen sodium is clearly visible

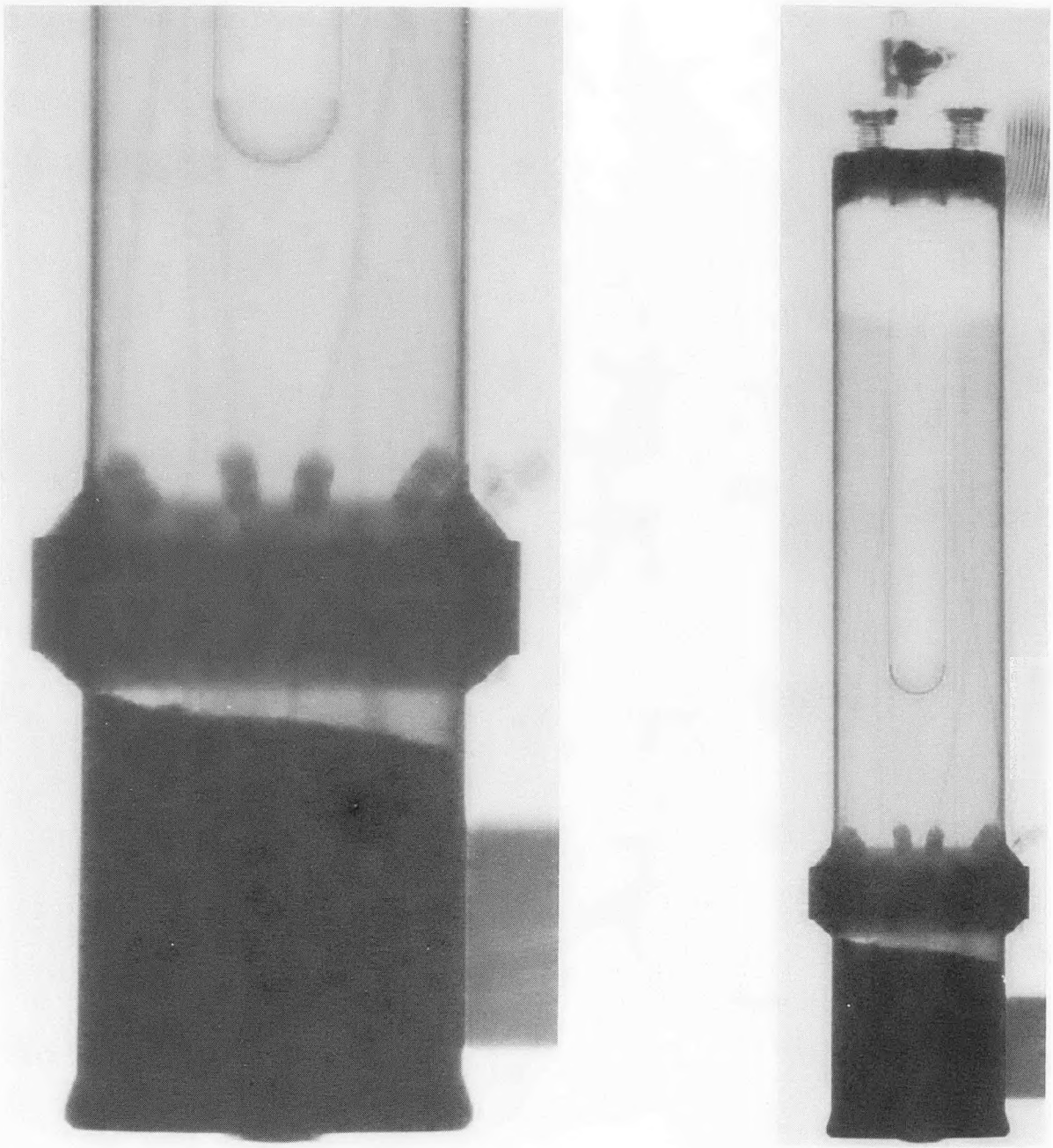

Figure 7. X-Ray of D-2 Taken 90° From Figure 6

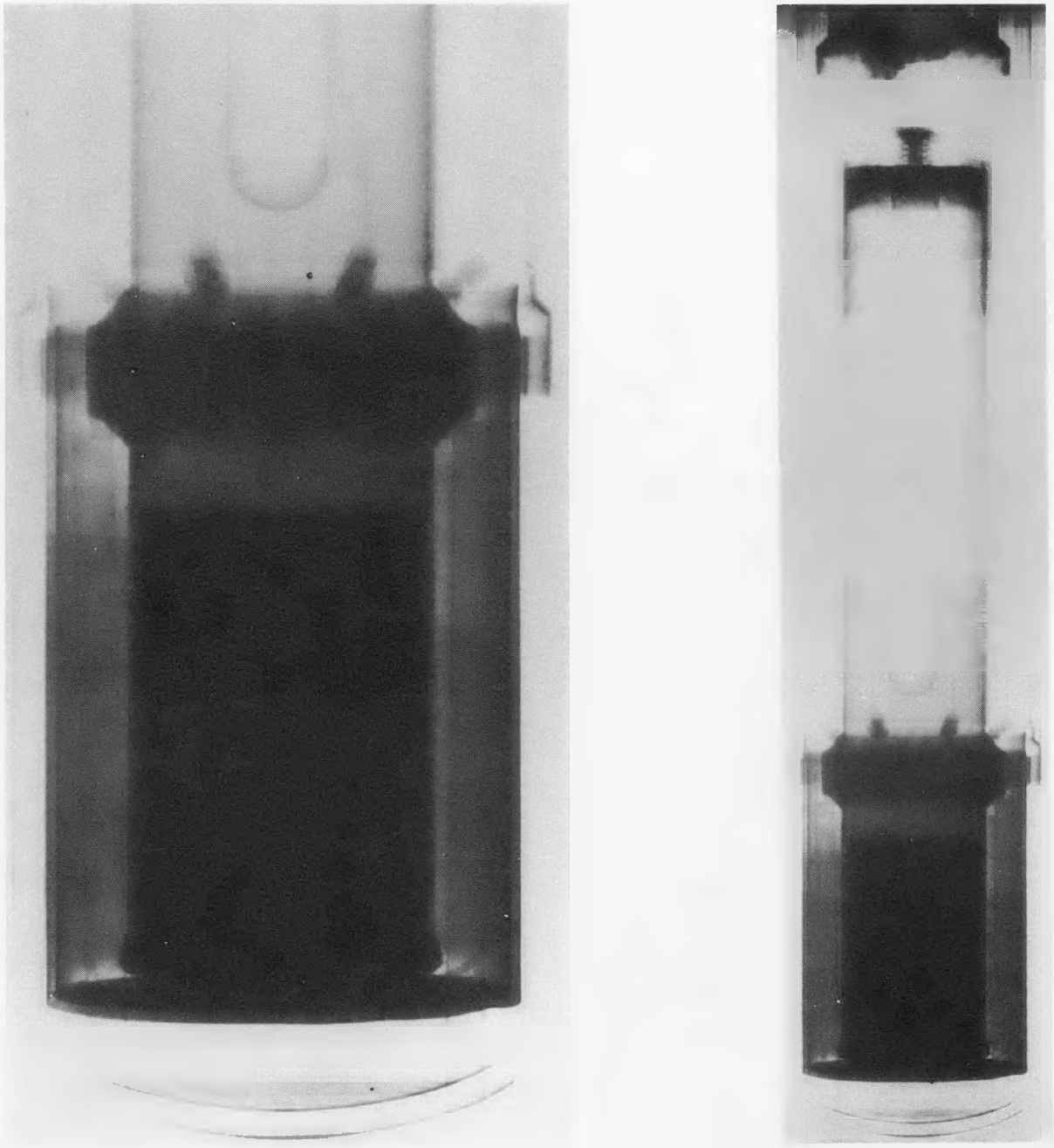

Figure 8. X-Ray of D-3 Experiment Capsule After Filling

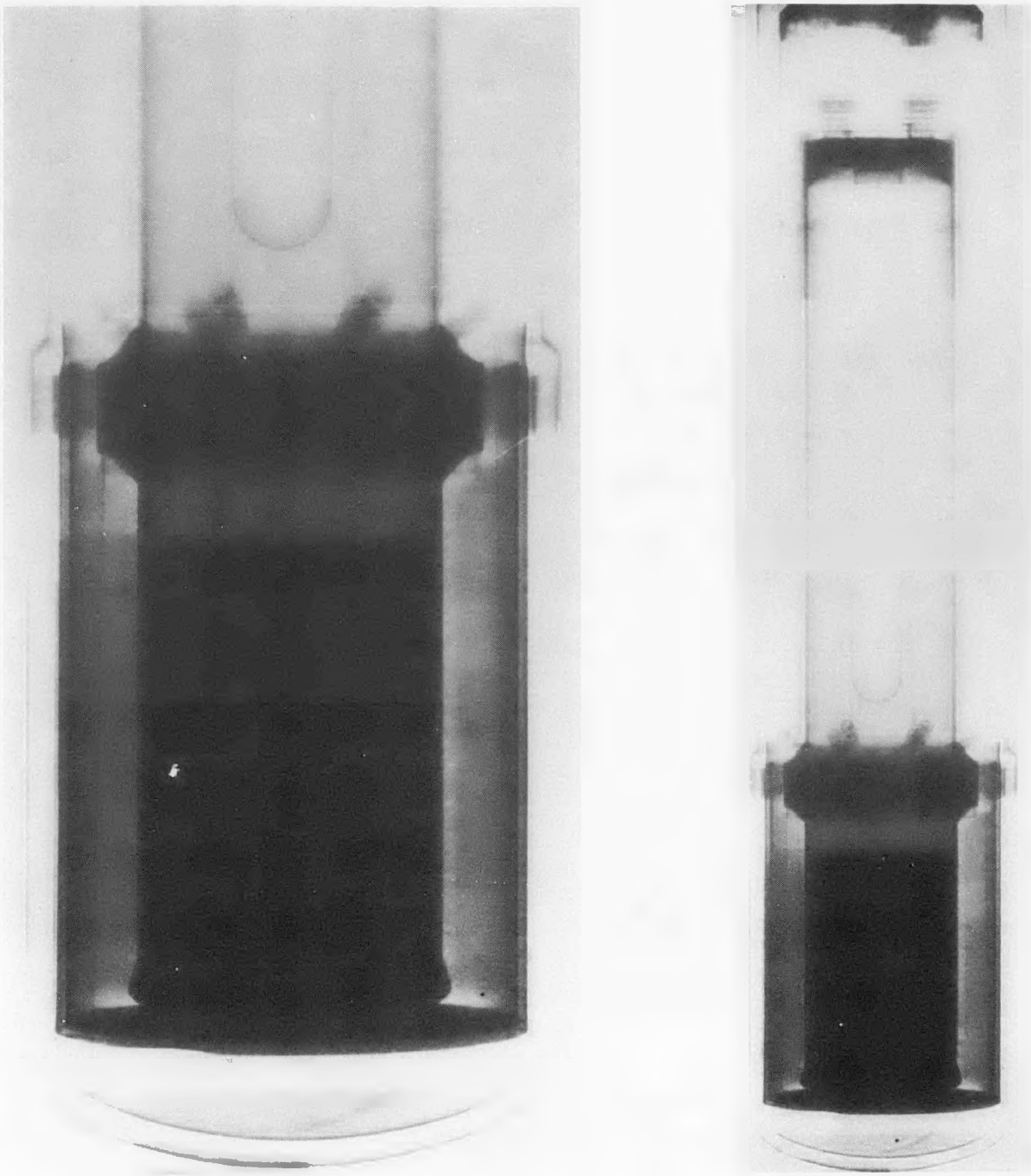

Figure 9. X-Ray of D-3 Taken 90° From Figure 8

At this latter power level, the entire lower half of the bed appeared to be dominated by two-phase convection: thermocouple M2 registered only about 10 K and M1 about 25 K below the saturation temperature. Shortly after reaching the 0.76 kW/kg level, thermocouple B2 suddenly began rising at a rate of approximately 25 K/minute. About one-half minute later, thermocouple B3 suddenly began a similar rise. After approximately 2 minutes, thermocouple B2 had reached 1177 K (904°C) and the dryout transient was terminated by decreasing the ACPR power to 10 kW. After determining that conditions had returned to normal, reactor power was raised to the equivalent of 0.69 kW/kg, followed 40 minutes later by 0.73 kW/kg. Conditions at these two power levels appeared stable and equilibrated, with all measured bed temperatures at, or near, saturation. After nearly 30 minutes at 0.73 kW/kg, the power was increased to 0.76 kW/kg. After about 5 minutes at this power level, thermocouple B2 suddenly began rising at about the same rate that it had during the previous dryout transient. It was followed, about one-half minute later, by thermocouple B3. After 1 minute, the rise rate of thermocouple B2 began decreasing, followed by B3. Four minutes after the start of the transient, thermocouple B2 had reached 1181 K (908°C), and its rise rate had reduced to a few degrees per minute. The transient was terminated after 4 1/2 minutes. During both of the dryout transients, thermocouple B1 (located at the junction of the bottom and the inside diameter) did not participate and registered a steady temperature of 1133 K (860°C) (saturation temperature).

The behavior observed during the first heating cycle is illustrated in Figure 10. The solid lines shown have been calculated using the Fourier conduction equation for a heat-generating medium with a constant thermal conductivity and with an upper bed surface temperature derived from the McDonald and Connolly[14] boundary layer formulation $Nu = 0.0785\ Ra_1^{0.32}$. This figure clearly demonstrates the transition from conduction behavior to two-phase behavior, followed by bed dryout.

Following the reduction in ACPR power terminating the second transient (10 kW is reached in about 10 s), thermocouples B2 and B3 were observed to drop in temperature, slowly at first and then more rapidly, approaching the temperature registered by thermocouple B1, which had itself begun a slow, steady decrease in temperature at a rate of 16 K/minute. At the time thermocouples B2 and B3 attained the same temperature as thermocouple B1 (approximately 1 1/2 minutes following the power reduction), they were decreasing very rapidly in temperature at rates estimated to be between 200 and 250 K/minute. Subsequent to attaining the same temperature as thermocouple B1, they began to decrease at the rate of 16 K/minute. The change from the initial slope to the latter slope was quite abrupt and is sharply defined on the temperature recordings. This abrupt change of slope appears to represent reentry of liquid sodium into the dryout zone.

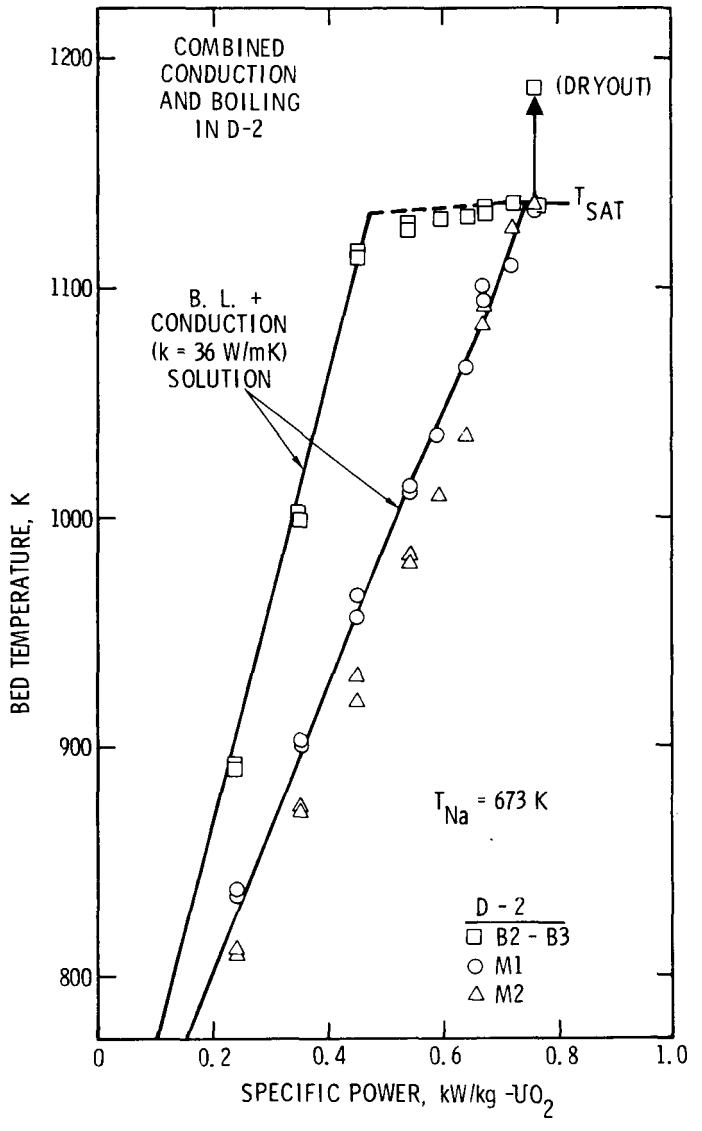

Figure 10. Combined Conduction and Boiling Behavior Observed During the First Heating Cycle of D-2.

The second heating cycle took place at a bulk sodium temperature of 873 K (600°C). As during the first cycle, the initial behavior at low power levels resembled the thermal conduction mode. However, shortly after a steady specific power of 0.40 kW/kg had been attained, all bottom thermocouples (B1, B2, and B3) began rising several degrees per minute. When they had risen nearly 20 K, thermocouple M1 (which had previously been registering about 80 K below the saturation temperature) suddenly rose very rapidly to the saturation temperature. (It is estimated that this took place in less than 10 s.) At the same time, thermocouple M2 (which had previously been registering about 100 K below the saturation temperature) suddenly rose very rapidly nearly 60 K (in about the same time as the M1 rise). Immediately following this unexpected transient, all bed thermocouples began slow decreases in temperature with some slow, coherent oscillations

of 5 to 10 K in magnitude. The above temperature excursions signalled an event which is subsequently referred to as a "disturbance", since the event appeared to alter the fundamental behavior of the bed.

Following this event, power was successively incremented upward to the ACPR maximum (corresponding to 1.28 kW/kg) without incident. All bed thermocouples continued to register within a few degrees of the saturation temperature of 1184 K (911°C), indicating that the predominant mode of bed heat transfer was two-phase convection.

The behavior observed during the second heating cycle of D-2 is illustrated in Figure 11, which was constructed using the same method as was used in Figure 10. This figure clearly shows the transition from conduction behavior to two-phase convection behavior, and includes the quasi-steady data points taken following the bed disturbance which is marked by an arrow.

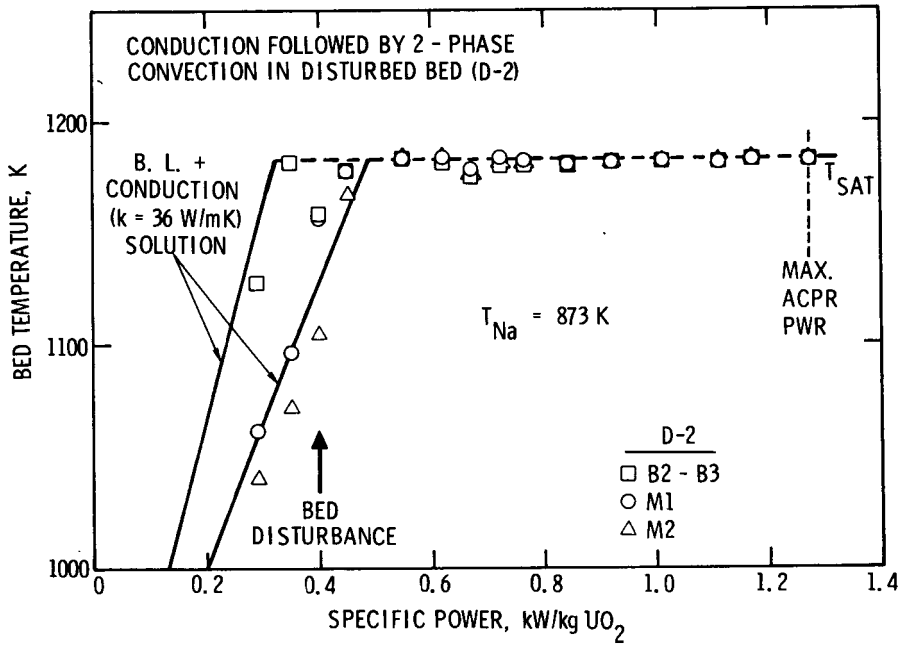

Figure 11. Conduction Followed by Two-Phase Convection in the "Disturbed" Bed as Observed During the Second Heating Cycle of D-2.

Since dryout did not occur during this second heating cycle, it was decided that the third heating cycle should repeat the conditions which produced dryout during the first heating cycle. Therefore, the bulk sodium temperature was reduced to 673 K (400°C) and upward power incrementation was begun, starting at an ACPR power corresponding to 0.69 kW/kg, and followed by 0.76 kW/kg. Indications of dryout were not observed.

The power continued to be successively incremented upward until the ACPR maximum (corresponding to 1.28 kW/kg) was achieved. All bed thermocouples continued to register within a few degrees of the saturation temperature, as they had on the previous heating cycle, and the cycle was completed without incident.

An additional heating cycle was attempted, but a malfunction in the helium cooling system prevented further operation; the experiment was therefore terminated.

D-3 Experiment

In the D-3 experiment, deep bed behavior was investigated using 7.29 kg of UO_2 which formed a bed about 158 mm deep. Three heating cycles at bulk sodium temperatures of (in order performed) 773, 673, and 873 K (500, 400 and 600°C) were employed to study the effect of sodium subcooling. High power levels were not achieved due to the occurrence of limiting temperatures during dryout.

Several instrumentation malfunctions slightly hindered the performance of D-3. Shortly after the start of the experiment, it was determined that thermocouple B2 was malfunctioning. Attempts to repair the thermocouple were of no avail. One of the capsule pressure transducers failed to operate from the start of the experiment; after 12 hours of nuclear operation, the thermocouple monitoring the helium coolant inlet temperature to the experiment capsule failed. Power diagnostic information from this point on in the experiment is therefore based on the earlier measurements.

Even at the start of the initial heating cycle at 773 K (500°C), when the power levels employed were quite low and before any boiling took place, the temperature readings within the lower quarter of the bed remained uniform, indicating that considerable single-phase convection was occurring in this region. The midbed thermocouples, M1 and M2, gave evidence of convection-augmented conduction. As the power continued to be incremented upward, the conduction influence decreased until, at about 0.27 kW/kg, all bed thermocouples registered the same temperature. At a specific power of 0.39 kW/kg, thermocouple B3 registered local dryout at the bottom of the bed. Some of the data taken during this heating cycle are shown in Figure 12, which illustrates the strong influence of convection in the lower part of the bed. The dryout transient indicated by thermocouple B3 was sustained for slightly over 8-1/2 minutes before the transient was terminated by the standard reactor-power decrease to 10 kW. All other thermocouples remained stable during the transient. During this period, the temperature in the dryout zone rose from 1193 K (920°C) to 1258 K (985°C). The initial rate of temperature rise was about 25 K/minute, but the rate at 8-1/2 minutes had decreased to about 2 K/minute.

Following the initial dryout, the power was again incremented upward to test the repeatability of the phenomenon. Again, at 0.39 kW/kg dryout occurred. All thermocouples except B3 remained stable during the transient. Dryout was allowed to continue for 18-1/2 minutes before being terminated by the standard reactor-power decrease. During this dryout transient, the temperature as indicated by thermocouple B3 rose from 1193 K (920°C) to 1263 K (990°C). The initial rate of temperature rise was about 20 K/minute, decreasing to about 1 K/minute at 18 minutes.

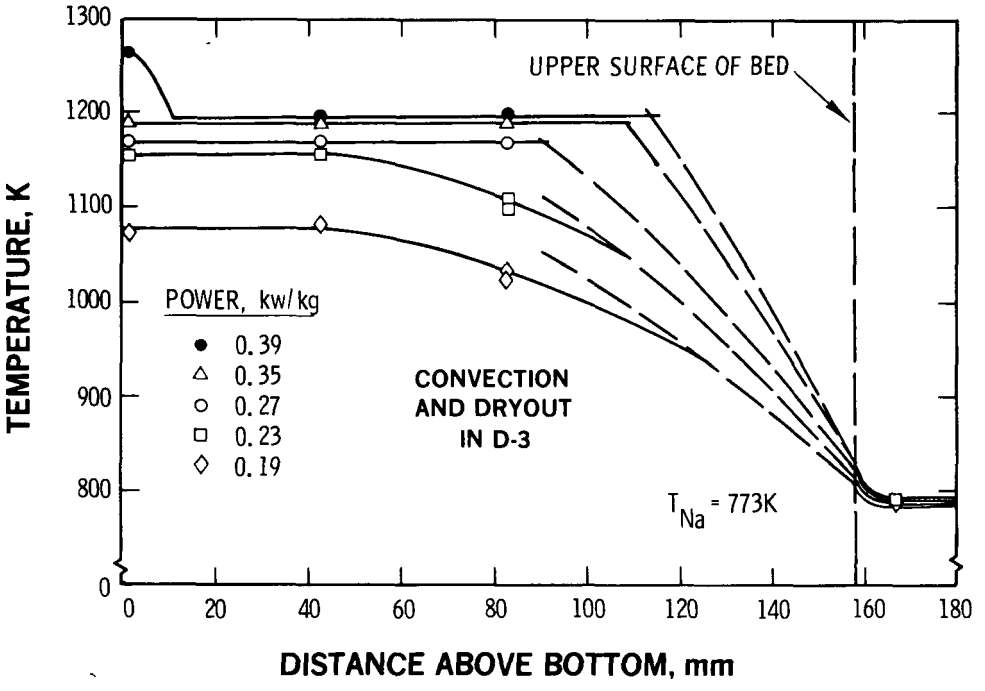

Figure 12. Typical Temperature Distributions Derived From Data Taken During the First Heating Cycle of D-3. The solid curves connect data points in the bed; the dashed curves and the curves above the bed were constructed from bed power, measured sodium temperatures, the McDonald-Connally[14] boundary layer formulation, and the thermal conduction solution for an effective bed conductivity of 36 W/m-K.

The second heating cycle was performed at a bulk sodium temperature of 673 K (400°C). The initial behavior was similar to that observed during the first heating cycle. Dryout was first observed at 0.41 kW/kg, about 11 minutes after reaching this power level, as indicated by thermocouple B3. Dryout was continued for 66 minutes before being terminated. All thermocouples except B3 remained stable during the transient. During this dryout transient, the temperature rose from 1158 K (885°C) to 1265 K (992°C). The initial rate of temperature rise was about 20 K/minute, while the final rate was only about 0.2 K/minute.

Following this transient, power was again incremented upward to test the repeatability of the phenomenon. After being at 0.39 kW/kg for 18 minutes, dryout again occurred. All thermocouples except B3 remained stable during the transient. Dryout was allowed to continue for 46 minutes at this power level. The temperature rose from 1155 K (882°C) to 1227 K (954°C). The initial rate of temperature rise was about 15 K/minute, decreasing to about 0.1 K/minute at 46 minutes. At this time, reactor power was increased slightly to a level corresponding to 0.41 kW/kg for a better comparison with the previous dryout transient. This resulted in a new temperature transient, as registered by the B3 thermocouple, which was continued for an additional 53 minutes (total: 99 minutes). During this transient, the temperature rose from 1227 K (954°C) to 1256 K (983°C), while the other bed thermocouples continued to register steady temperatures of about

1156 K (883°C). The initial rate of temperature rise was slightly more than 1 K/minute, and the final rate was about 0.1 K/minute.

At 99 minutes after the start of the dryout transient, the power was intentionally decreased rapidly to a value corresponding to 0.30 kW/kg. Thermocouple B3 (in the dryout zone) registered an initial slow decrease in temperature which gradually steepened. At 109 minutes after the start of dryout (10 minutes after the power reduction), the rate of temperature decrease had reached about 4 K/minute, with the temperature now at 1213 K (940°C). This rate of decrease continued until about 120 minutes (21 minutes after power reduction), when, with the temperature at 1177 K (904°C), a very steep temperature decrease (estimated at 100 K/minute) began which ended in a steady plateau at 1147 K (874°C) (saturation temperature) one minute later. This abrupt termination of the decrease appears to represent reentry of liquid sodium into the dryout zone. This sequence of transients is shown in Figure 13. The previous dryout transients observed during the D-3 experiment, including the initial dryout transient of this sequence, are shown in Figure 14. Table II summarizes all the dryout transients of experiments D-2 and D-3.

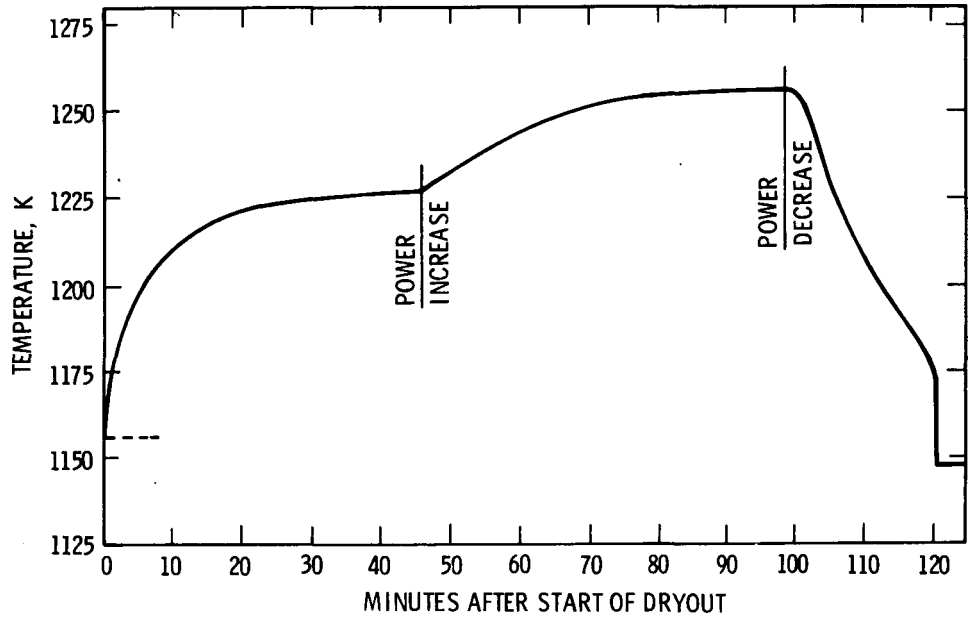

Figure 13. Dryout Nos. 4 and 5 and Termination, as Observed During the D-3 Experiment

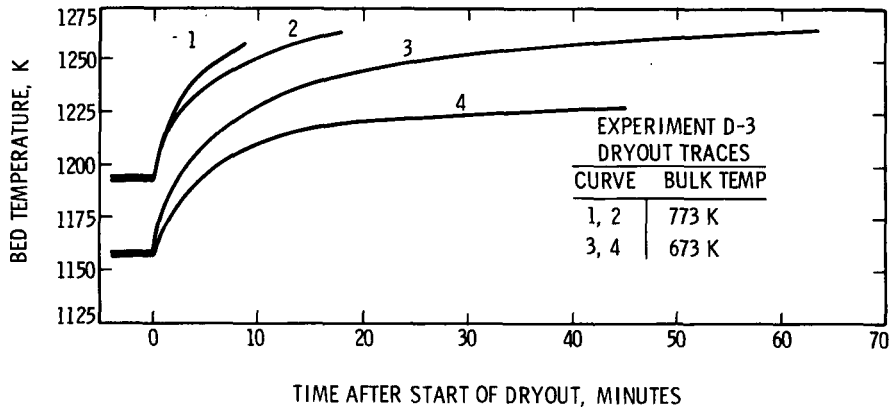

Figure 14. Dryouts Nos. 1, 2, 3, and 4 as Observed During the D-3 Experiment

TABLE II

Dryout Parameters, D-2 and D-3

Parameter	D-2		D-3				
	No. 1	No. 2	No. 1	No. 2	No. 3	No. 4	No. 5
Bulk Sodium Temperature, K	673.	673.	773.	773.	673.	673.	673.
Specific Power Level, kW/kg	0.76	0.76	0.39	0.39	0.41	0.39	0.02*
Starting Temperature, K	1135.	1135.	1193.	1193.	1158.	1155.	1227.
Ending Temperature, K	1177.	1181.	1258.	1263.	1265.	1227.	1256.
Total Temperature Rise, K	42.	46.	65.	70.	107.	72.	29.
Duration, Minutes	2.	4.5	8.5	18.5	66.	46.	53.
Initial Temperature Rise Rate, K/min	25.	25.	25.	20.	20.	15.	1.
Final Temperature Rise Rate, K/min	10.	3.	2.	1.	0.2	0.1	0.1
Delay Time Before Start of Dryout, min	--	5.	9.	17.	11.	18.	NA**
Initial Rise Rate/Adiabatic Rise Rate	0.18	0.18	0.36	0.29	0.27	0.21	0.28

*Increment of power above previous level.

**Not applicable; dryout in progress.

Following the above-described sequence, the third heating cycle was begun with the bulk sodium temperature at 873 K (600°C). The power level was incremented upward to the equivalent of 0.34 kW/kg, where further power increase was halted by the attainment of limiting vessel temperatures. No dryout occurred. At this power, all bed thermocouples registered about 1212 K (939°C). The third heating cycle was terminated at this time and the bulk sodium temperature was lowered to 773 K (500°C) where a control run was executed, repeating a power run performed at the start of the experiment. All thermocouples repeated their earlier readings to within 3 or 4 K, indicating that the thermal properties of the particle bed had not changed during the conduct of the experiment. Following this, the D-3 experiment was terminated.

Analysis and Interpretation of Results

The experiments demonstrate that a number of heat-transfer regimes are possible in self-heated urania particle beds in liquid sodium, and that the regimes apparently can coexist. In the liquid saturated beds, conduction, single-phase-convection, two-phase-convection, and convection-augmented-conduction regimes have been identified. The temperature rise rate in the liquid-voided zone decreased steadily in these experiments, indicating that a steady- or quasi-steady-state condition was being approached, although the approach was very slow and a steady-state was never attained. As may be seen in Table II, even the initial temperature rise rate is a fraction of the adiabatic (maximum possible) rise rate. The dryout phenomena is in general repeatable with the same threshold power level, but the temperature transient reoccurs with somewhat reduced rates and reduced quasi-equilibrium temperatures. Dryout terminates shortly after the power level is reduced significantly below the threshold value.

It appears quite likely that temperatures high enough to melt urania (~3130 K), or even to sinter particulate urania of this size distribution (~2670 K)[15], could only be achieved at power levels substantially exceeding those which produced dryout during these experiments. This contrasts to assumptions widely held, prior to these experiments, that dryout in self-heated oxide fuel particulate would eventually produce melting of the fuel material. This assumption led previous researchers to consider dryout as the limiting parameter in debris-bed stability--with dryout marking the beginning of reactor vessel destruction by high temperature debris. It now appears that, while dryout may be a necessary condition for the occurrence of fuel melting, it may not always be a sufficient condition. In particular, in these experiments, quasi-equilibrium dryout states were achieved, and a modest power increase (dryout No. 5, Table II) led to another quasi-equilibrium state at slightly higher temperature levels. It seems clear, however, that this process will ultimately end at some considerably higher power level.

The dryout data obtained during these experiments is compared with previously published work in Figure 15. The dryout data points from the present experiments are given together with dryout data points (squares) for similarly-sized UO_2 particles in sodium from the fluid-heated experiments of Gabor et al.[12] (The lower solid curve through the (ANL) data is the least-squares

fit reported in Reference 12.) While no drastic disagreement is present in the data, the ANL data at large bed loadings tend toward lower power levels than data taken during D-3. This is apparently not attributable to porosity (sodium volume fraction), since the porosities reported by ANL were larger than the 0.43 measured for D-3.

The other curve in Figure 15 is computed from the "maximum coolable debris bed depth" equations reported by Dhir and Catton[16], based upon their extensive experiments with a variety of inductively-heated particles in several fluids (not including urania and sodium). The break in the curve corresponds to the transition from their shallow-bed correlation to their deep-bed correlation. A diameter of 500 μm, corresponding to the author's "mean particle diameter" for the D-3 distribution, and a porosity of 0.43 were employed in calculating the plotted correlations.

Hardee and Nilson[17] have formulated a dryout prediction which does not employ a correlation constant. In their model (Figure 16) the heat generated in the two-phase region is absorbed by two mechanisms: a temperature increase to the boiling temperature in the liquid flowing downward in the region; and, in the rising fluid region, a phase change to the vapor state. Based upon energy and continuity equations written at a location near the top of the bed where all the upward flowing fluid has become vapor and employing Darcy flow relations, they derived the following expression for the heat-generation rate at dryout:

$$pL\,(1-\epsilon) = \frac{\rho_\ell g K \ell}{\rho \nu_v} \quad \frac{\left[1 + C_\ell \left(T_B - T_C\right)/\ell\right]}{\left[1 + \sqrt{\nu_\ell/\nu_v}\right]^2} \tag{1}$$

A difficulty with the Hardee-Nilson forumlation is an uncertainty in the location of the cross-section where the energy and continuity equations are applied. This allows some uncertainty in the bed height (L) over which Eq. (1) applies.

Observations at incipient dryout during the D-2 and D-3 experiments indicate that the two-phase region is actually nearly isothermal (e.g., see Figure 14). The temperature difference $(T_B - T_C)$ is observed to occur primarily in the conduction region at the top of the bed. These two observations can be utilized in a reformulation of the problem originally solved by Hardee and Nilson. First, the location of the cross-section where the energy and continuity equations are applied is redefined such that the applicable bed height (L) is reduced to correspond to the region in which two-phase flow occurs. This reduced height (L^*) is found by application of the conduction equation with an effective bed conductivity (k_B):

$$L^* = \left\{\left[\frac{c}{(1-\epsilon)\rho}\right]^2 - \frac{2k_B\left(T_B - T_C\right)}{p\,(1-\epsilon)\rho}\right\}^{1/2} . \tag{2}$$

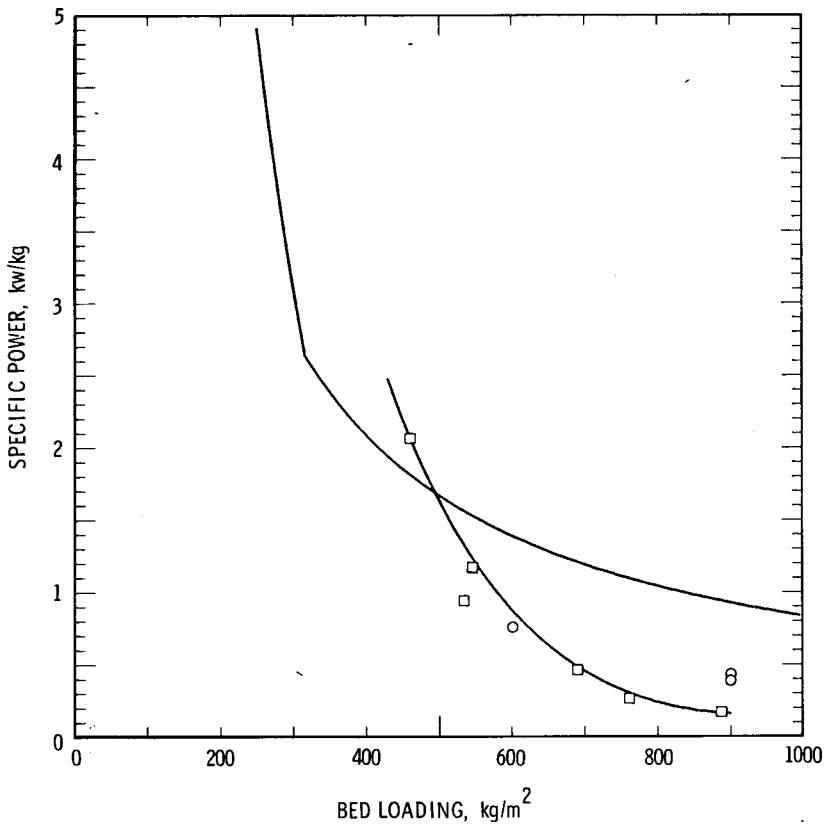

Figure 15

Dryout Data and Correlations. The circle data points are from the D-2 and D-3 experiments, while the squares are the fluid-heated data of Gabor et al.[12] The lower solid curve is the least-squares fit reported in Reference 12; the other curve is the Dhir-Catton[16] correlation.

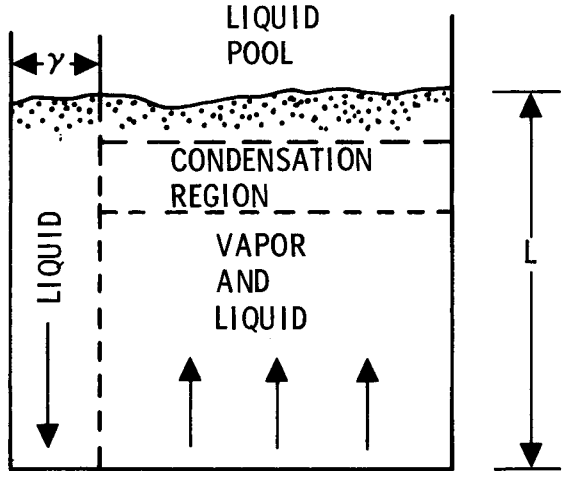

Figure 16. Liquid and Vapor Flow in the Two-Phase Regime (from Reference 17).

Second, the temperature increase in the liquid flowing downward in the two-phase region is reduced to zero in correspondence with observation. Application of these two changes to the initial conditions of the problem is illustrated in Figure 17.

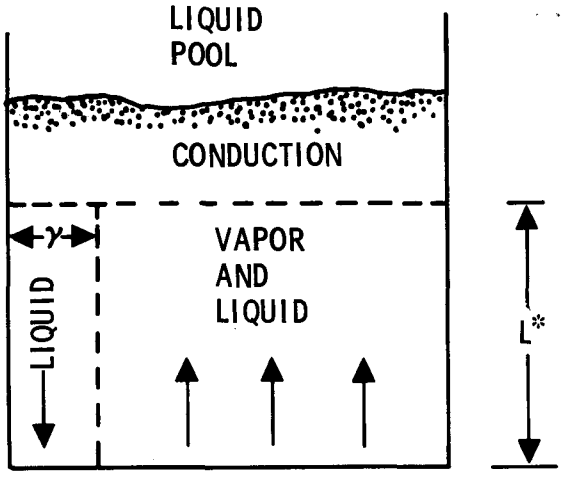

Figure 17. Reformulation of the Liquid and Vapor Flow in the Two-Phase Regime

Following the line of the Hardee-Nilson derivation with these changes results in a new expression for the heat-generation rate at dryout:

$$(pc)^2 - 2\,p\,k_B\left(T_B - T_C\right)(1-\epsilon)\rho = \left[\frac{\rho_\ell\, g K_\ell}{\nu_v\left(1+\sqrt{\nu_\ell/\nu_v}\right)^2}\right]^2 \tag{3}$$

Direction application of Eq (3), as in the case of the Hardee-Nilson expression, is limited by the fact that the temperature at the top of the bed, T_C, is accessible only indirectly through a boundary-layer analysis. However, an approximation may be formed by assuming the boundary-layer temperature drop at the top of the bed to be zero. This gives:

$$(pc)^2 - 2\,p\,k_B\,\Delta T_s\,(1-\epsilon)\,\rho = \left[\frac{\rho_\ell\, g K_\ell}{\nu_v\left(1+\sqrt{\nu_\ell/\nu_v}\right)^2}\right]^2 \tag{4}$$

The application of Eq. (4) to the D-2 and D-3 experiments is illustrated in Figure 18, where the three dryout data points are shown as squares. All three solid curves correspond to Eq. (4) with an effective bed conductivity of 36 W/m-K, based on D-2 measurements (see above). The lower two curves utilize a permeability of 200 darcys, which is in the range of deep bed permeabilities observed in previous measurements.[2] The subcooling used for the lowest curve is 400 K; for the intermediate curve a value of 500 K was used. The upper curve shows the effect of an increased permeability of 400 darcys, with a subcooling of 500 K. (Due to the method of forming the D-series beds,[2] the measured permeabilities should be regarded as lower bounds.)

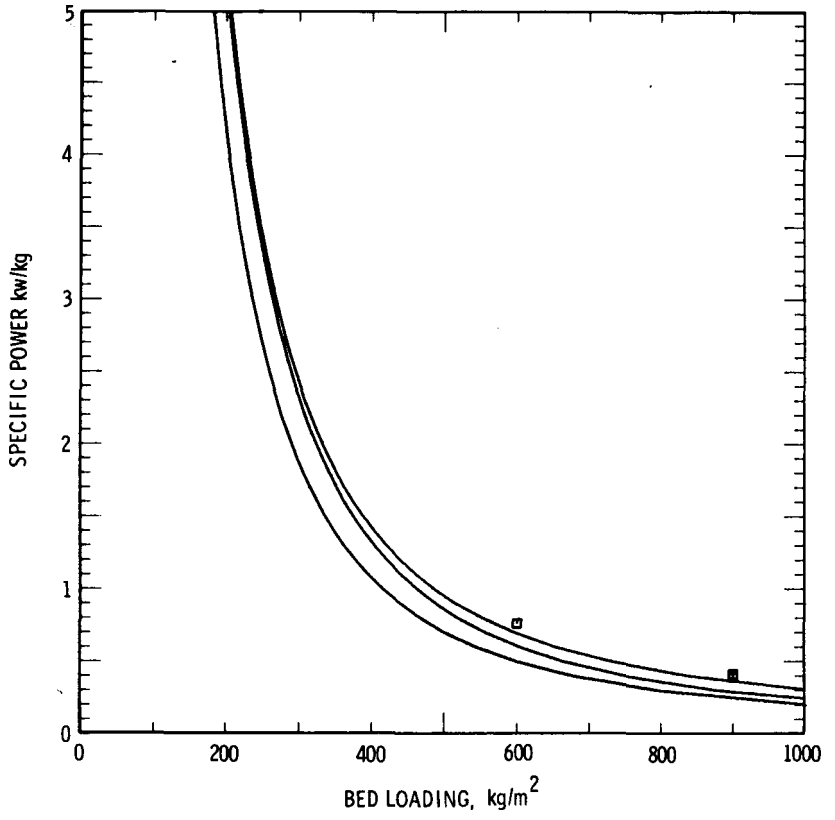

Figure 18. The Dryout Formulation of This Work (solid curves) Compared With Data Points for the D-2 and D-3 Experiments. The parameter values giving the three curves are given in the text.

In the above one-dimensional analysis, it was assumed that the bottom of the bed is adiabatic. However, during the reactor scenario, it is unlikely that the surfaces supporting the bed will provide sufficient insulation to be considered truly adiabatic; some heat will therefore be transferred downward from the bed. This downward heat transfer will necessarily occur in the presence of a stable (inversion) temperature gradient wherein higher temperatures (and smaller fluid densities) overlay lower temperatures (and larger fluid densities), inhibiting convection. At incipient dryout, the upper boundary of this downward conduction region will be at the saturation temperature, while the lower boundary at the bottom of the bed will be at a temperature less than the saturation temperature. Dryout will thus occur at a location displaced upward from the bottom of the bed by the thickness of this conduction region. Consideration of this added region in the analysis given above results in a modified reduced height (L^*) -- previously given in Eq. (2) -- which may be written as

$$(L^*) = \left\{ \left[\frac{c}{(1-\epsilon)} \right]^2 - \frac{2k_B \left(T_B - T_C\right)}{p\,(1-\epsilon)\,\rho} \right\}^{1/2} - \left[\frac{2k_B \psi \left(T_B - T_C\right)}{p\,(1-\epsilon)\,\rho} \right]^{1/2} \qquad (5)$$

in which ψ represents the fraction of the temperature difference $(T_B - T_C)$ which exists between the upper and lower bounds of the downward conduction zone. Straightforward development, analogous to that given above, then leads to the following expression for the heat-generation rate at dryout:

$$(pc)^2 - 2k_B\left(T_B - T_C\right)p\rho(1-\varepsilon) = \left\{\frac{\rho_\ell\, g\kappa L}{\nu_v\left[1+\sqrt{\nu_e/\nu_v}\right]^2} + \left[2k_B\,\psi\left(T_B - T_C\right)p\rho(1-\varepsilon)\right]^{1/2}\right\}^2 \quad (6)$$

An example of the application of this equation is given in Figure 19, where, in analogy with Eq. (4), it has been assumed that the boundary layer temperature difference above the top of the bed is zero. Figure 19 has been constructed for a subcooling, ΔT_s, of 400 K, an effective conductivity (k_B) of 36 W/m-K, a permeability (κ) of 200 darcys, a porosity (ε) of 0.43, and values of ψ ranging from 0.0 to 0.8. It thus gives an example of the influence of bottom cooling of debris which is predicted by this analysis. For all bed loadings, the heat-generation rate at dryout for these conditions is increased by approximately a factor of two with ψ = 0.8, and by approximately a factor of 1.6 with ψ = 0.4.

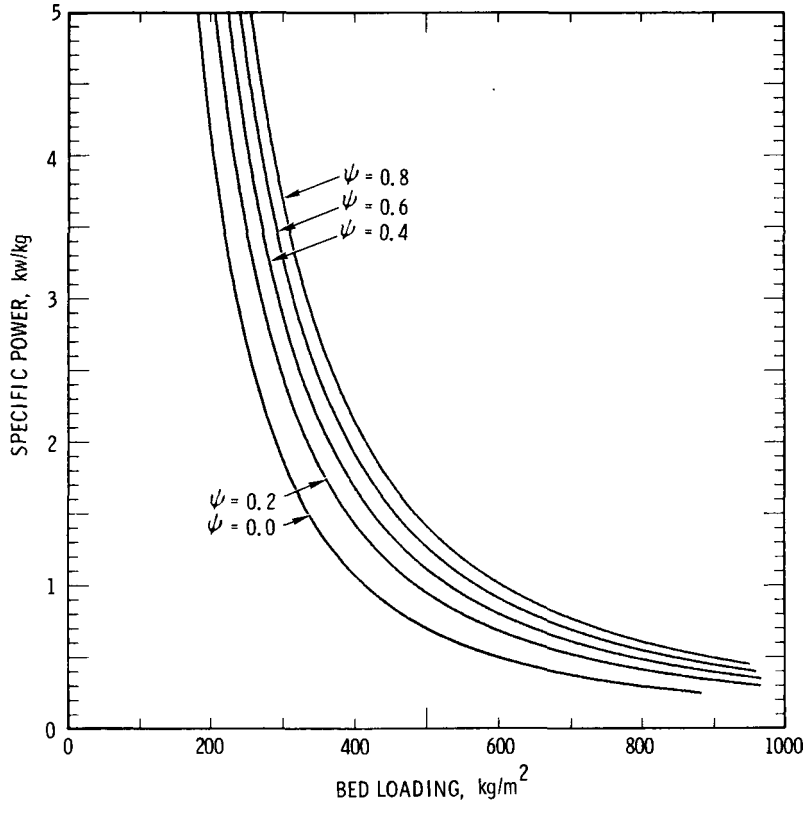

Figure 19. Example of the Influence of Bottom Cooling on Debris Bed Dryout. ψ is the fraction of the subcooling ΔT_S which exists across the downward conduction zone. Other parameters are given in the text.

From the general behavior observed in these experiments, we surmise that the power being generated within the dryout zone is unidirectionally transferred out of the zone by a process which may be approximated by a one-dimensional conduction-type process. (Radiation-heat transfer may augment the process, but is not directly considered in this report.) The dryout process in D-2 apparently began at the center of the bed and progressed radially outward, enveloping the B3 thermocouple location within a minute after the start of the transient. It did not, however, reach the B1 thermocouple location within the rather short duration of these initial dryout transients. This implies that the phenomenon was not exactly one-dimensional during these experiments, and further implies that dryout may have begun a few minutes before being detected in the D-3 experiment, due to the absence of B2 thermocouple data. In the following analysis, however, a one-dimensional slab is assumed for ease in computation.

If it is assumed that the dryout zone is established quickly with a constant thickness in the vertical direction, a plausible explanation of the temperatures observed during dryout would be given by the temperature response at a fixed location (z) within a medium of thickness ($\mathbf{Z}$) which is suddenly subjected to internal power generation at a constant rate (q) (per unit volume), while one boundary ($z = \mathbf{Z}$) of the medium is maintained at a fixed temperature corresponding to the sodium saturation temperature. The other boundary ($z = 0$) of the medium is considered adiabatic. For a simple conduction model of this process (Figure 20), we write:

$$\frac{\partial \theta}{\partial t} = \alpha \frac{\partial^2 \theta}{\partial z^2} + \frac{q}{\rho c}$$

for the temperature elevation $\theta(z,t)$ above the sodium saturation temperature. The initial condition

$$\theta(z,0) = 0$$

and boundary conditions

$$\frac{\partial \theta(0,t)}{\partial z} = 0, \quad \theta(\mathbf{Z},t) = 0 \ ,$$

complete the specification of the problem for adiabatic and isothermal boundaries.

The solution for this problem is given by[18]

$$\frac{\theta(z,t)}{q\mathbf{Z}^2/k} = \frac{1}{2}\left[1 - \left(\frac{z}{\mathbf{Z}}\right)^2\right] - 2\sum_{n=0}^{\infty} \frac{(-1)^n}{\left(\lambda_n \mathbf{Z}\right)^3} e^{-\alpha\lambda_n^2 t} \cos \lambda_n z \qquad (7)$$

where the eigenvalues are:

$$\lambda_n Z = (2n + 1)\pi/2, \quad n = 0, 1, 2, 3, \ldots,$$

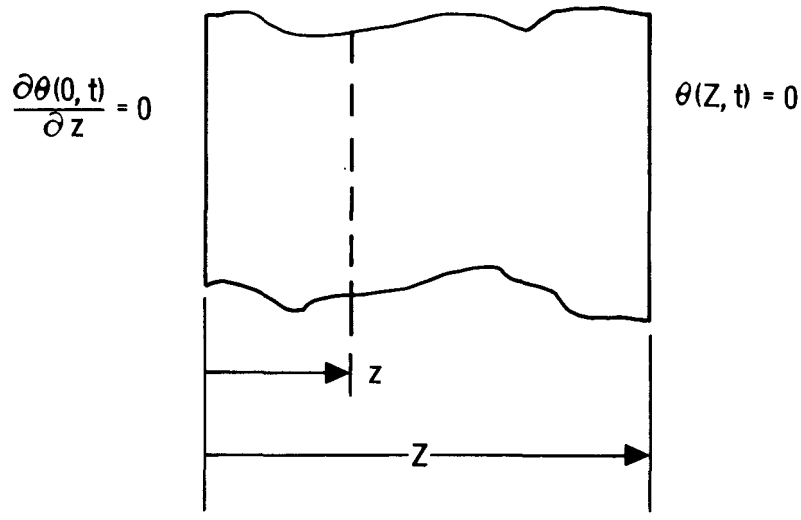

Figure 20. Conduction Model of Dryout Zone, Initial Hypothesis. Bottom of the bed is at left.

Figure 21 shows temperature elevations at a particular value of z versus time given by the above solution for three values of Z, namely 5, 10, and 15 mm. (The particular value of z chosen is 1.5 mm, which corresponds approximately to the vertical distance to the center of the thermocouple sensing the dryout temperature transient.)

In this analysis, the power-generation rate is 2.28 (10^3) kW/m^3 of bed volume, which corresponds to 0.4 kW/kg of UO_2 in the D-3 experiment. The (constant) values of thermal conductivity chosen were 1.73 and 0.86 W/m-K, corresponding to one-half and one-quarter, respectively, of the value for solid UO_2. With regard to the thicknesses chosen in the D-3 experiment, the lack of any dryout-associated signal from the B1 thermocouple (see Figure 5) provides an upper bound (~40 mm) to the vertical thickness of the zone. Superimposed on this figure is a typical temperature transient observed during dryout on the D-3 experiment.

Comparison of the analytical curves with the experimental curve in Figure 21 shows their markedly different character. With possible values for the thickness and thermal conductivity of the dryout zone, the analytical curves achieve a relatively rapid response and an early equilibrium. In contrast, the typical experimental curve given shows a relatively slow apparent response and no evidence of equilibrium within a 15-minute time frame. Thus, this comparison strongly suggests that an alternate hypothesis is required to explain the results obtained from the experiments.

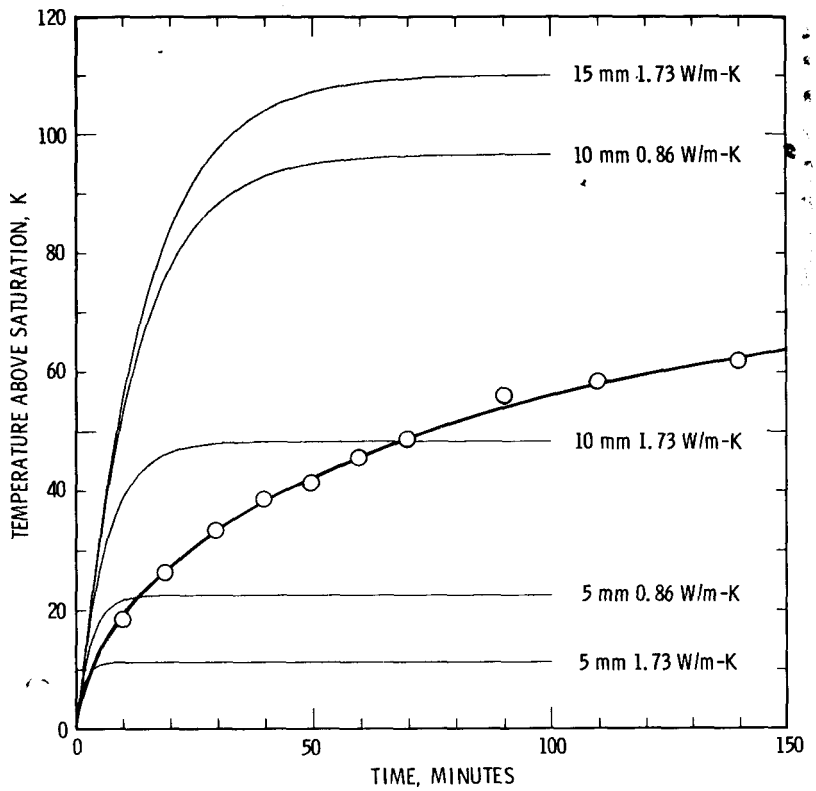

Figure 21. Calculated temperature elevations (Eq. (7)) vs time at 1.5 mm above the bottom of the bed for three thicknesses of dryout zone, compared with observed temperature transient during dryout of the D-3 experiment (circles).

An alternate theory which requires only minor alteration of the original hypothesis is obtained if we assume that the thickness of the dryout zone is established more slowly. This is conceptually equivalent to considering the thickness (**Z**) in the original mathematical formulation (Eq. (7)) a variable function of time (t), (Figure 22). Recalling that, for a general function F (X, t), where X is a function of t,

$$\frac{dF}{dt} = \frac{\partial F}{\partial X}\,\frac{dX}{dt} + \frac{\partial F}{\partial t} \quad ;$$

we may therefore write (symbolically) the formulation for the temperature response (θ_2) at a fixed location in a medium of variable thickness, **Z** (t):

$$\theta_2\,(\mathbf{Z},t) = \int_0^t \left[\frac{\partial \theta}{\partial \mathbf{Z}}\,\frac{d\mathbf{Z}}{dt'} + \frac{\partial \theta}{\partial t'}\right] dt' \qquad (8)$$

Applied to the solution of the original problem, this forumulation yields

$$\frac{\theta_2(Z,t)}{q/K} = \int_0^t \left\{ \frac{dZ}{dt'} - 2\sum_{n=0}^{\infty} \frac{(-1)^n}{(\lambda_n Z)^3} e^{-\alpha\lambda_\eta^2 t'} \left[\left[2\frac{dZ}{dt'} + \alpha\lambda_n^2 \left(2t'\frac{dZ}{dt'} - Z \right) \right] \right.\right.$$

$$\left.\left. \cos \lambda_n z + \lambda_n z \frac{dZ}{dt'} \sin \lambda_n z \right] \right\} dt' \qquad (9)$$

where it is to be understood that **Z** and its derivative are functions of time.

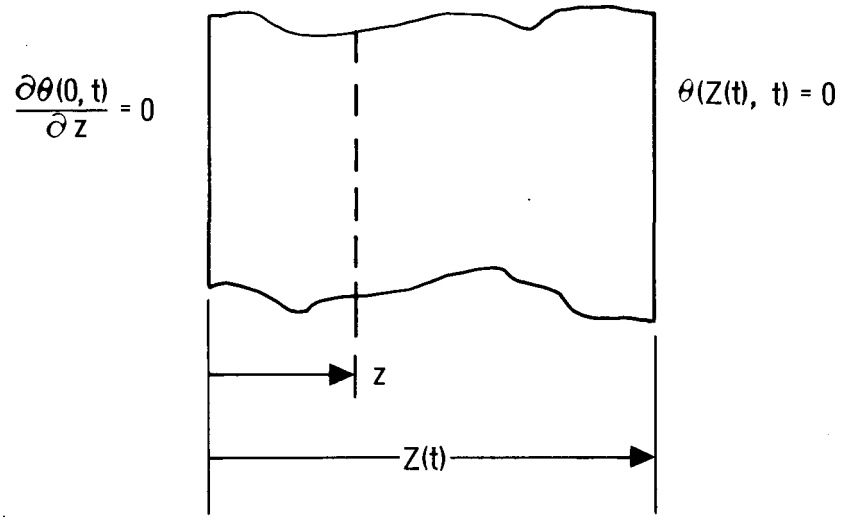

Figure 22. Conduction Model of Dryout Zone, Second Hypothesis

A necessary test of the hypothesis consists in finding **Z** such that the above integral gives values which match the observed dryout responses. Since Eq. (9) is not in general analytically integrable, a numerical integration technique was employed. Also, in order to allow precision in the taking of the derivative, an analytical formulation of **Z** was used. Because of the shape of the observed temperature response curves, and to allow sufficient freedom in the matching effort, the function chosen for **Z** was

$$Z = A\left(1 - e^{-\beta t}\right) + B\left(1 - e^{-\gamma t}\right) \quad . \qquad (10)$$

In Figures 23 through 26, the solution to Eq. (9), with the constants in Eq. (10) taken as given in Table III, is compared with data points from dryout Nos. 1 through 4 for the D-3 experiment. The resulting **Z** are given in Figure 27. All curves for **Z** show similar characteristics: a rapid initial rise, followed by a very shallow approach toward an equilibrium geometry.

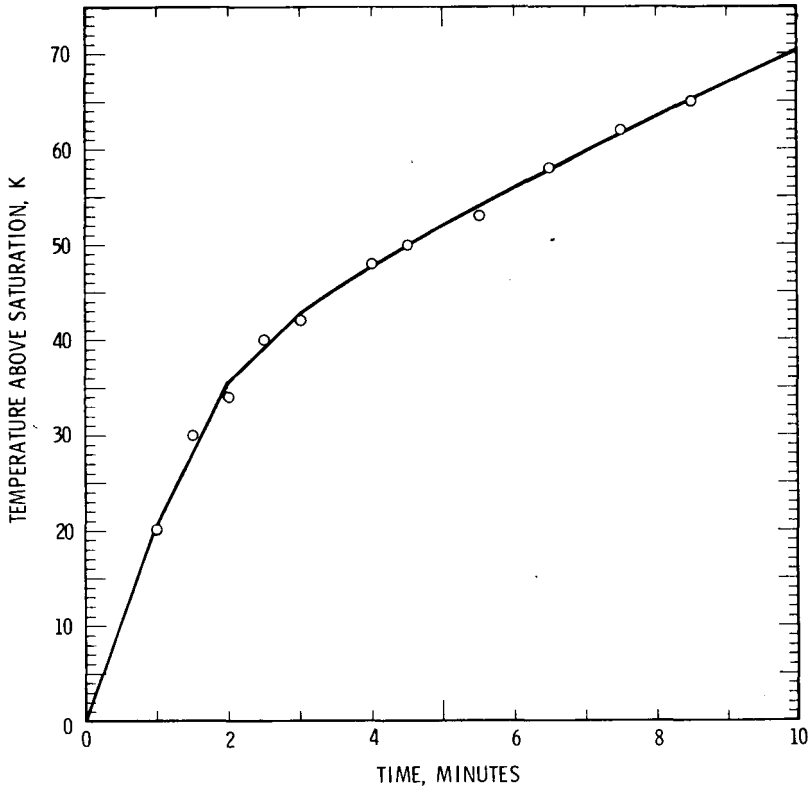

Figure 23. Calculation (solid line), Using Eq. (9) and (10), Compared With Data Points From Dryout No. 1, D-3 Experiment

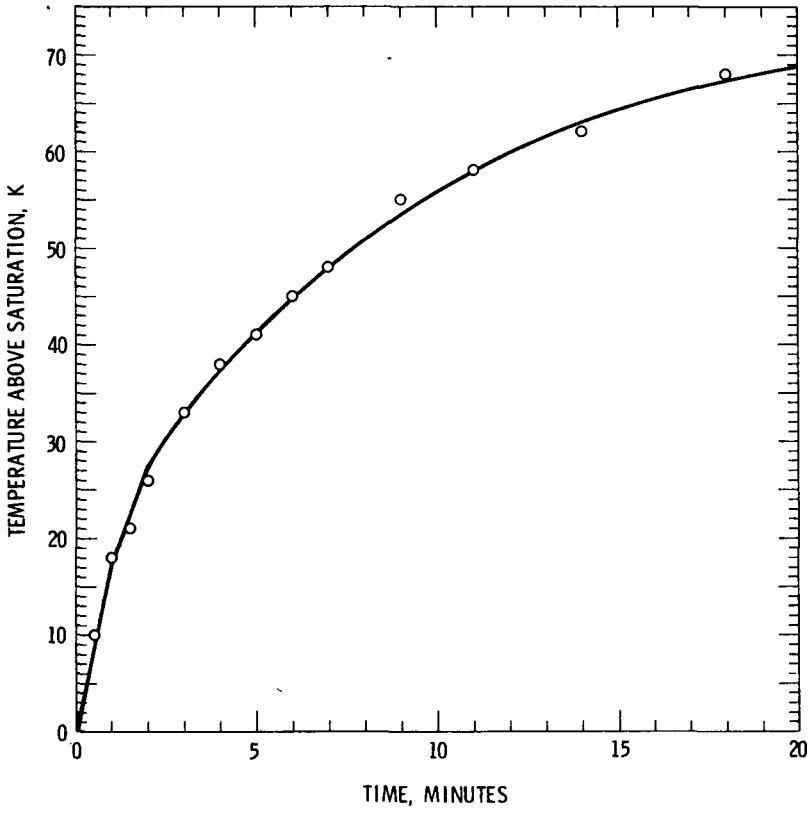

Figure 24

Calculation (solid line), Using Eq. (9) and (10), Compared With Data Points From Dryout No. 2, D-3 Experiment.

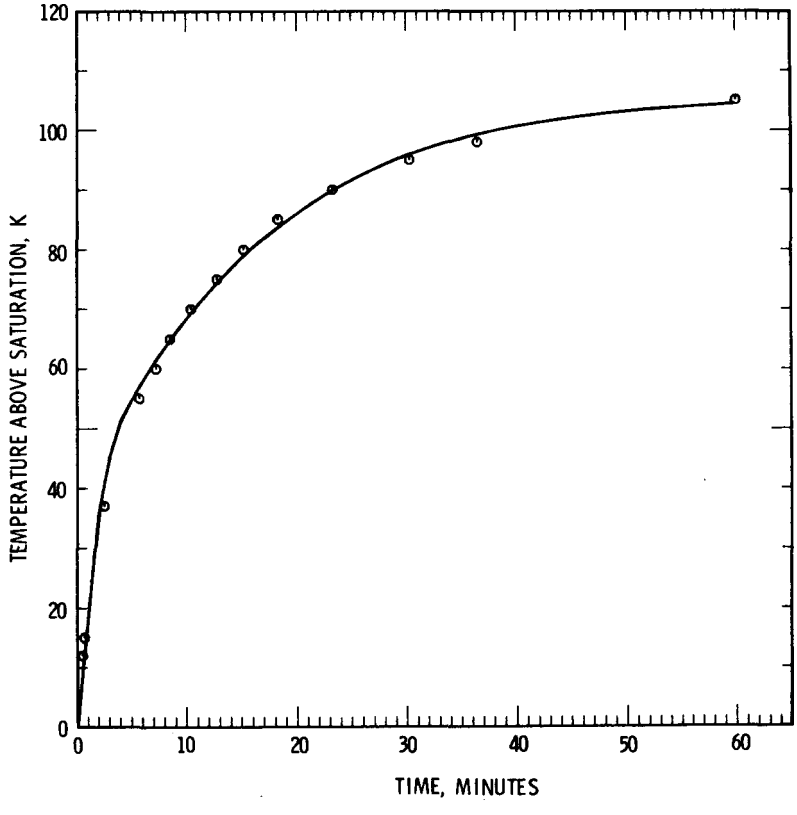

Figure 25

Calculations (solid line), Using Eq. (9) and (10), Compared With Data Points From Dryout No. 3, D-3 Experiment.

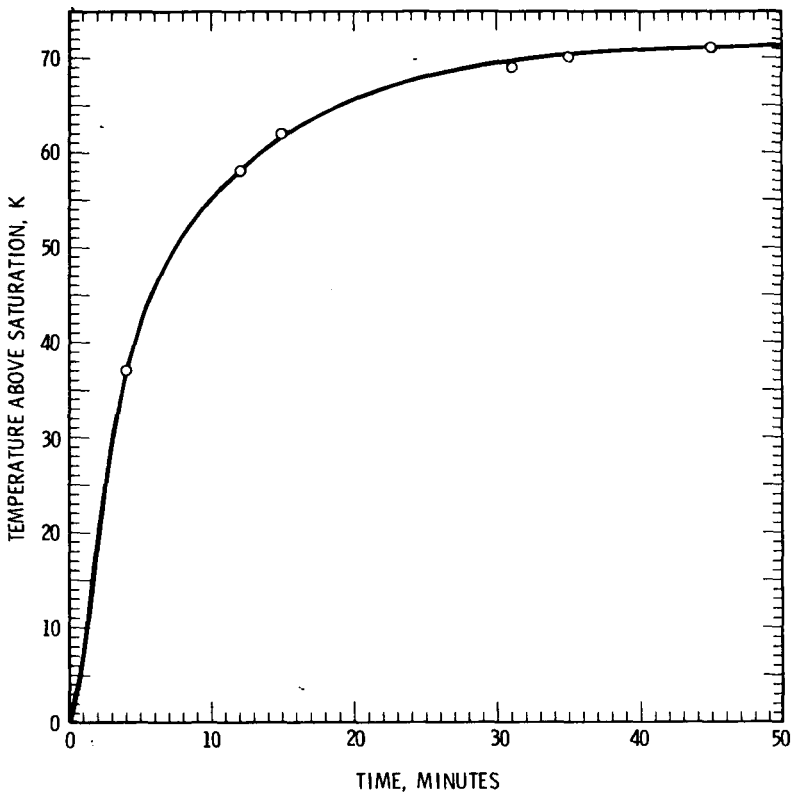

Figure 26

Calculation (solid line), Using Eq. (9) and (10), Compared With Data Points From Dryout No. 4, D-3 Experiment

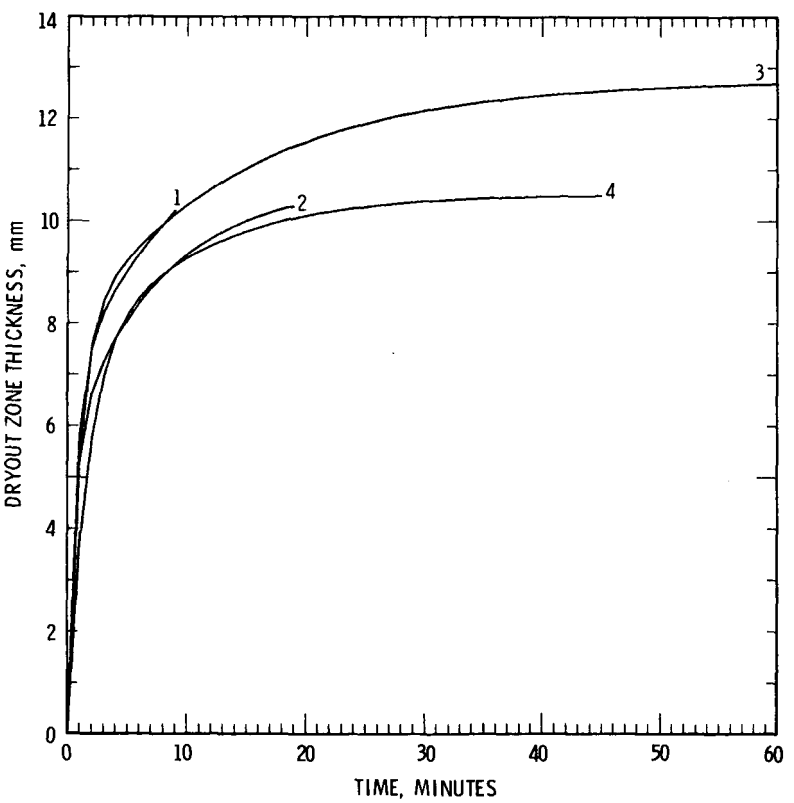

Figure 27

Values of Variable Dryout Zone Thickness (Z) Calculated for Dryouts No. 1 Through No. 4 for the D-3 Experiment

TABLE III

Constants in Thickness Equations

Dryout No.	A	B	β	γ
1	$7.00(10^{-3})$	$6.70(10^{-3})$	$2.40(10^{-2})$	$1.20(10^{-3})$
2	$5.60(10^{-3})$	$5.10(10^{-3})$	$3.10(10^{-2})$	$2.20(10^{-3})$
3	$7.80(10^{-3})$	$4.95(10^{-3})$	$1.80(10^{-2})$	$1.17(10^{-3})$
4	$6.95(10^{-3})$	$3.85(10^{-3})$	$1.10(10^{-2})$	$1.75(10^{-3})$

It is not possible to show that the curves given in Figure 27 are unique in the mathematical sense. It cannot be shown at this time that boundary movement, as embodied in the function Z, is entirely responsible for the observed temperature behavior. In particular, variation of the effective thermal conductivity of the zone has not been considered in the above analysis. Nevertheless, this explanation for the behavior is plausible, and is appealing because of the obvious necessity for the dryout zone to achieve some thickness over time in order to provide even a rudimentary explanation of the observations, and because of the failure of a simpler initial hypothesis to adequately explain those observations.

An additional consideration generated by this model of dryout behavior is the deviation from the equilibrium temperature distribution within the dryout zone. Obviously, if the zone expansion is slow enough, thermal quasi-equilibrium will prevail in the zone; rapid zone expansion would be expected to produce nonequilibrium distributions. In the former case, the temperature distribution would be given by the first term on the right-hand side of Eq. (7), with **Z** representing the expanding thickness of the zone. A measure $\xi(\mathbf{Z},t)$ of the nonequilibrium is thus given by the difference between this function and Eq. (9),

$$\xi(\mathbf{Z},t) = \frac{1}{2}\left[1 - \left(\frac{z}{\mathbf{Z}}\right)^2\right] - \int_0^t \mathbf{Z}\left\{\frac{d\mathbf{Z}}{dt'} - 2\sum_{n=0}^{\infty}\frac{(-1)^n}{\left(\lambda_n \mathbf{Z}\right)^3}\, e^{-\alpha\lambda_n^2 t'}\right.$$

$$\left.\left[\left[2\frac{d\mathbf{Z}}{dt'} + \alpha\lambda_n^2\left(2t'\frac{d\mathbf{Z}}{dt'} - \mathbf{Z}\right)\right]\cos\lambda_n z + \lambda_n z\frac{d\mathbf{Z}}{dt'}\sin\lambda_n z\right]\right\} dt' \qquad (11)$$

where it is to be understood that Z and its derivative are functions of time (t).

For z taken at the thermocouple location given above, evaluation (with the previously used assumptions) shows ξ to be negligibly small for the four expansions given in Figure 27. This tends to support the contention that zone expansion is not driven by thermal imbalance within the zone; rather, the zone is thermally stable for the conditions of the calculation and the heat generated within the zone is transferred in a quasi-steady manner to the upper boundary of the zone.

This effect is examined further in Figure 28, which was generated using the derived expansion for dryout transient No. 4. The upper curve represents the power generated in the dryout region. The two lower curves represent the power which is absorbed in performing the work of displacing the liquid sodium column upward (lowest curve) and in vaporizing the sodium supplied to the expanding zone (intermediate curve). The first 60 s of this figure is shown in expanded form in Figure 29, which emphasizes that, after a few seconds, the absorbed power has decreased to a few percent or less of the power generated within the dryout zone. The small amplitude of the absorbed power (both in the absolute and in the relative sense), combined with the fact that the region is thermally in quasi-equilibrium, means that dryout does not significantly alter the power transferred -- only the mode of its transfer.

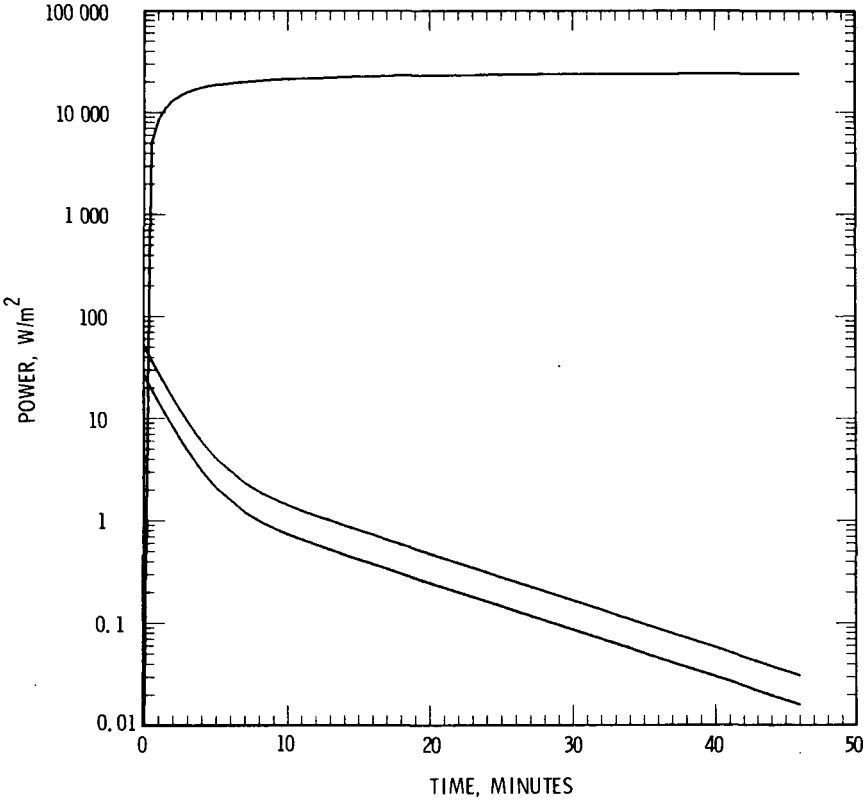

Figure 28. Power Partitioning During Dryout as Calculated for Dryout Expansion No. 4 (Figure 27). The upper curve is the power generated in the dryout zone; the intermediate curve is the power absorbed in phase change; and the lowest curve is the power used in performing the work of displacing the liquid sodium column upward.

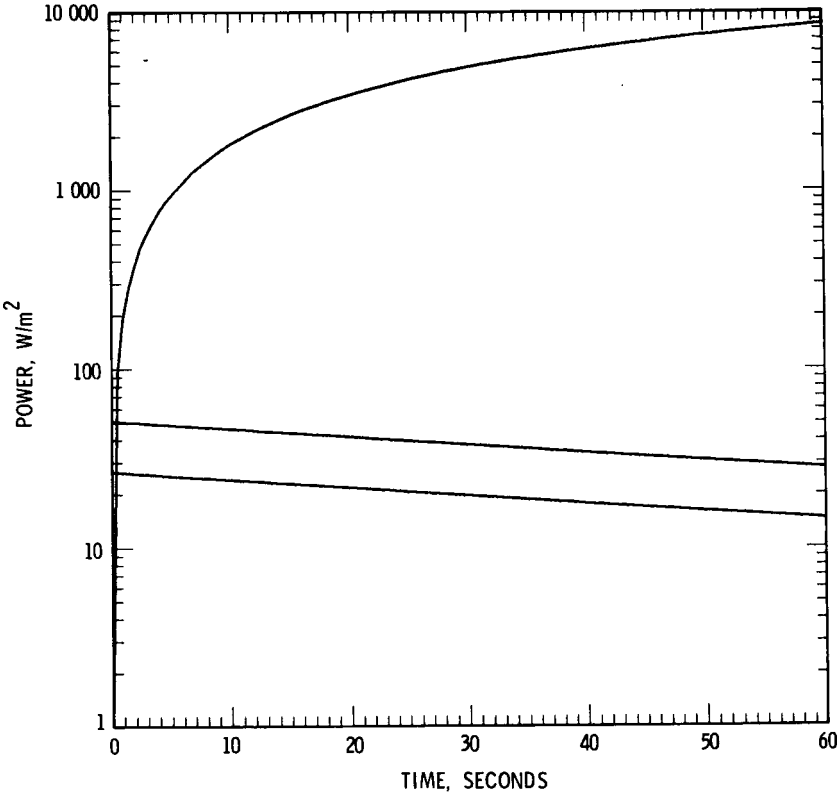

Figure 29. Expanded Plot Showing the First Minute of Figure 28

It is desirable to project the results of the dryout data and this analysis to power levels above those which induce dryout. In dryout No. 5, it was observed that a 6% increase in power during dryout resulted in a 29 K (40%) increase in temperature elevation (Table II). For a conductivity of 36 W/m-K, this corresponds to an equilibrium thickness increase of ~2 mm (18%). Although this appears to imply that the dryout zone thickness increases at a rate in excess of the power increase rate, the data is obviously insufficient to support reliable extrapolation. The present analysis of the dryout phenomenon (Eq. (1), (2), and (3)) implies a hyperbolic relationship between heat-generation rate (specific power) and L^* (the effective convection length). Thus, in Eq. (3), as dryout reduces L^*, higher power levels can be sustained, a fact which is in agreement with experiment and physical intuition. Extrapolated, however, the hyperbolic relationship fails by projecting infinite power at $L^* = 0$. A sound basis for predicting heat-generation rates which will result in potentially destructive temperatures (as applied to the fast-reactor scenario) therefore awaits more extensive experimentation into power regimes beyond the threshold dryout level.

Summary and Conclusions

In the D-2 experiment (bed loading 600 kg/m^2), liquid voiding by vapor generation (dryout) at the bottom of the bed occurred during the first heating cycle at 673 K, which limited the specific power to 0.76 kW/kg. The dryout was repeatable. During the second heating cycle (at 873 K), a bed "disturbance" at 0.4 kW/kg apparently altered the bed sufficiently to allow subsequent operation, without dryout, to the power limit of the ACPR -- corresponding to 1.28 kW/kg. Operation during the third cycle (a repeat of first cycle conditions at 673 K) was also performed without dryout to the power limit of the ACPR.

In the D-3 experiment (bed loading 900 kg/m^2), dryout occurred during the first heating cycle at 773 K, limiting the specific power to 0.39 kW/kg. The dryout was repeated. Dryout occurred at 0.41 kW/kg during the second heating cycle (at 673 K), and was repeated at a power level of 0.39 kW/kg. Both dryouts were maintained for long periods of time (66 minutes and 46 minutes, respectively). At the 46-minute mark during the second dryout of this cycle, the power was raised to 0.41 kW/kg, and maintained for an additional 53 minutes, for a total of 99 minutes of continuous dryout. The power increase resulted in an increase in temperature, but the rate of increase became very small near the end of the dryout sequence. No bed "disturbance" was observed, and the control run just prior to termination of the experiment showed the thermal properties of the bed unchanged by operation of the experiment.

During all experiment sequences, the maximum temperature observed was 1265 K at the bottom of the containment vessel; it is believed that this represents the maximum temperature that occurred during the experiments.

The experiments demonstrate that conduction, single- and two-phase convection, and the convection-augemented-conduction heat-transfer regimes are possible in self-heated urania particle beds in liquid sodium, and that the regimes apparently can coexist.

Temperatures in the conduction-dominated upper zones of self-heated urania particle beds are well-predicted by a conduction model with an effective thermal conductivity on the order of half the value for sodium alone, coupled with a boundary-layer solution in the bulk sodium above the bed.

Following the immediate initial temperature rise during dryout, the temperature-rise rate in the dryout zone decreased steadily, indicating a slow approach to a steady- or quasi-steady-state condidtion. The largest temperature-rise rate observed did not exceed 40% of the adiabatic (maximum possible) rise rate; most temperature rises took place at rates which are very small fractions of adiabatic rates. These experiments, therefore, tend to demonstrate that the threshold power to produce dryout in medium-depth beds and deep beds of 100 - to 1000-μm urania does not lead to extremely high temperatures or to melting of the fuel. An increase to a higher-than-threshold power level produces an increase in the quasi-equilibrium temperature, but it is not

possible to reliably extrapolate the data to deduce the power level at which very high temperatures or fuel melting would occur.

The vapor-channel model of incipient debris-bed dryout developed earlier[12,16] is primarily applicable to reactor conditions in which the bulk coolant is at its saturation temperature. The review given above in the "Introduction" indicates that the so-called Loss-of-Heat-Sink (LOHS) scenario is the most likely accident sequence yielding bulk saturation conditions after a time lapse of $\geq 10^4$ s following successful scram of the reactor. At this time, the decay-heat source has decreased to about 1% of operating power, easing the cooling problem for decay-heated debris. For Loss-of-Flow (LOF) and Transient-Overpower (TOP) accidents, substantial subcooling of the bulk coolant is generally assumed during postaccident heat removal; this is the condition addressed by the D-series experiments.

The model of threshold dryout proposed here does not incorporate vapor channels. It does incorporate the conduction zone and nearly-isothermal, two-phase convection observed during the highly-subcooled experiments. Based on the Hardee-Nilson[17] formulation, it does not rely on data-correlation. It agrees reasonably well with the data generated during D-2 and D-3, and has been extended to cover the case of a nonadiabatic lower boundary (Eq. (6)). At the large subcoolings employed in the experiments, the amount of subcooling did not have much effect on the inception of dryout; however, the formulations developed (Eq. (3), (4), and (6)) predict a relatively small effect of subcooling on deep bed dryout (for example, the lower two curves in Figure 18).

The review of the decay-heat source term indicates that, as applied to debris, local sodium boiling (which could produce dryout) cannot occur until about 16 s after reactor scram, at which time the source term has decreased to about 5%. More importantly, acquisition of the melting temperature of steel requires 33 s (source: 4.5%). Urania melting temperature would be reached after 88 s (source: 3.7%), according to these very conservative calculations. These times can be usefully compared with the significant delays (up to 18 minutes) which were observed prior to the onset of dryout at threshold power levels in these experiments.

Although no direct evidence on bed leveling is available from these experiments, the domination by conduction-mode heat transfer of the upper regions of the beds (in highly subcooled sodium) strongly suggests that vapor-bubble penetration to the upper surface of the beds is negligible up to dryout-threshold power levels in beds which have not experienced a "disturbance". For "disturbed" beds or those in saturated sodium, vapor-induced particle movement at the upper bed surface may provide leveling potential.

From the simplified analysis reported in the "Introduction," it is clear that the settling process will result in beds of increased permeability and, most importantly, the resulting particle-size separation produced will yield a higher permeability near the bottom of the bed, thus reducing the chance of dryout by promoting convection at that location. Future experiments are planned to investigate these effects.

A one-dimensional synthesis of the thermal behavior during dryout shows that the observed temperature transients are due to increasing thickness of the dryout zone rather than to thermal equilibration of a rapidly-formed zone. In addition, the analysis shows that the zone is in approximate thermal equilibrium during its expansion. Vapor generation and the work of displacing the sodium upward absorb little energy during the dryout process; thus, dryout does not significantly alter the power transferred -- only the mode of its transfer. The main result of dryout is the shortening of the convection flow paths in the region above the dryout zone, leading to a more stable hydrodynamic regime.

A number of unexplained phenomena remain as motivation for additional study and experimentation. These include the phenomena associated with the occurrence of the "disturbance" during the second heating cycle of D-2, the significant delay (up to 18 minutes) observed prior to the onset of dryout at threshold power levels, and the reduced temperature rise observed when dryout was repeated under apparently identical conditions (Figure 14).

Further work on self-heated urania beds in sodium is planned to explore higher power levels in shallow beds, above-threshold dryout power levels, naturally settled beds, effect of particle sizes, and the addition of nonheated particles.

References

1. A.S. Benjamin, "Draft Work Plan for Containment Analysis, "Sandia Laboratories Report (10/13/77) to be published.

2. J.B. Rivard, Debris Bed Studies and Experiments at Sandia Laboratories, SAND78-0299, Sandia Laboratories, 1978.

3. J.B. Rivard, "First In-Reactor Experiment With Simulated LMFBR Debris Bed," ANS Winter Meeting, San Francisco, CA, Transactions, 27, pp. 653-4, 1977.

4. J.B. Rivard, "Preliminary Results From Initial In-Pile Debris Bed Experiments," Third Post-Accident Heat Removal Information Exchange, Argonne National Laboratory, Chicago, IL., Proceedings, ANL-78-10, pp. 49-61, 1978.

5. B.D. Turland and R.S. Peckover, "The Distribution of Fission Product Decay Heat," Third Post-Accident Heat Removal Information Exchange, Argonne National Laboratory, Chicago, IL., Proceedings, ANL-78-10, pp. 17-25, 1978.

6. T.E. Murley, L.S. Tong, and G.L. Bennett, "Summary of LWR Safety Research in the USA," International Conference on Nuclear Power and Its Fuel Cycle, Salzburg, Austria, May 2-13, 1977, U.S.N.R.C. NUREG-0234, 1977.

7. American Nuclear Society, "Decay Energy Release Rates Following Shutdown of Uranium-Fueled Thermal Reactors," ANS Standard 5.1, 1971.

8. M.S. Kazimi, S.S. Tsai, and R.D. Gasser, Post-Accident Fuel Relocation and Heat Removal in the LMFBR, BNL-NUREG-50603, Brookhaven National Laboratory for the U.S.N.R.C., 1977

9. C.K. Chan, T.K. Min, and D. Okrent, A Look at Alternate Core Disruption Accidents in LMFBRs, PB-267577, NUREG-0259, University of California at Los Angeles for U.S.N.R.C., 1977.

10. R.A. Bari, M.A. Klenin, W.T. Pratt, and Y.H. Sun, Preliminary Assessment of the Meltdown Progression of the Loss-of-Heat-Sink Accident with Scram in the LMFBR, BNL-NUREG-23137, Brookhaven National Laboratory for the U.S.N.R.C., 1977.

11. R.A. Bari, H. Ludewig, W.T. Pratt, and Y.H. Sun, Material Relocation and Recriticality Assessment for the Loss-of-Heat Sink Accident in the LMFBR, BNL-NUREG-23432, Brookhaven National Laboratory for the U.S.N.R.C., 1977.

12. J.C. Gabor, E.S. Sowa, L. Baker, Jr., and J.C. Cassulo, "Studies and Experiments on Heat Removal from Fuel Debris in Sodium," CONF-740401-P2, ANS Fast Reactor Safety Meeting, pp. 823-844, April 3, 1974.

13. J.A. Brammer, "Mobile Helium Cooling Loop System for In-Reactor PAHR Experiments," 1977 Winter Meeting ANS, San Francisco, CA, Transactions, 27, pp. 651-3, 1977.

14. J.S. McDonald and T.J. Connolly, "Investigation of Natural Convection Heat Transfer in Liquid Sodium," Nuclear Science and Engineering, 8, pp. 369-377, 1960.

15. H.G. Plein and G.A. Carlson, "Debris Bed and Sacrifical Materials Interaction at High Temperatures," to be presented at ANS Winter Meeting, Washington, D.C., Nov. 12-17, 1978.

16. V.K. Dhir and I. Catton, Study of Dryout Heat Fluxes in Beds of Inductively Heated Particles, NUREG-0262, University of California at Los Angeles for the U.S. Nuclear Regulatory Commission, 1977.

References (cont)

17. H.C. Hardee and R.H. Nilson, "Natural Convection in Porous Media with Heat Generation," Nuclear Science and Engineering, 63, pp. 119-32, 1977

18. V.S. Arpaci, Conduction Heat Transfer, Addison-Wesley Publishing Company, Reading, MA, 1966.

APPENDIX A

D-2 Data Summary

Thermocouple Readings (°C)

Bed Power (kW)	Bulk Sodium	Bed Bottom*	M1	M2	Comment
1.15	398.0	620.0	564.0	539.0	
1.15	404.0	618.0	563.0	538.0	
1.70	400.0	728.5	629.0	598.0	
1.70	400.0	728.0	630.0	599.0	
2.20	400.0	842.5	693.0	657.0	
2.20	400.0	841.0	684.0	647.0	
2.65	400.0	855.0	741.0	709.0	
2.65	400.0	854.0	738.0	707.0	
2.88	400.0	858.0	764.0	736.0	
3.10	400.0	858.0	792.0	763.0	
3.25	400.0	861.0	829.0	819.0	
3.25	400.0	860.0	822.0	811.0	
3.50	400.0	863.0	836.0	854.0	
3.72	400.0	863.0	860.0	865.0	Dryout No. 1, Bottom Temp is Saturation
3.50	400.0	861.0	825.0	838.0	
3.61	400.0	863.0	839.0	847.0	
3.72	400.0	863.0	860.0	865.0	Dryout No. 2, Bottom Temp is Saturation
1.15	400.0	643.5	569.0	554.0	
1.40	600.0	855.0	788.0	767.0	
1.70	600.0	907.5	824.0	800.0	
1.95	600.0	886.5	883.0	832.0	
2.20	600.0	904.5	905.0	895.0	Postdisturbance
2.70	600.0	911.0	912.0	911.0	
3.00	600.0	909.5	911.0	910.0	
3.25	600.0	903.5	905.0	903.0	
3.50	600.0	909.0	910.0	909.0	
3.72	600.0	909.5	910.0	909.0	
4.10	600.0	907.5	908.0	907.0	
4.50	600.0	908.5	909.0	908.0	
4.92	600.0	909.5	909.0	909.0	
5.38	600.0	910.0	910.0	909.0	
5.70	600.0	910.0	910.0	910.0	
6.20	600.0	911.0	911.0	910.0	
3.50	400.0	849.5	850.0	818.0	
3.72	400.0	852.5	853.0	852.0	
4.10	400.0	849.5	850.0	842.0	
4.50	400.0	847.5	847.0	818.0	
5.38	400.0	853.0	853.0	846.0	
6.20	400.0	850.5	849.0	846.0	

*Average of B2 and B3

APPENDIX B

D-3 Data Summary

Thermocouple Readings (°C)

Bed Power (kW)	Bulk Sodium	B3	B1	M1	M2	Comments
0.63	205.0	440.0	441.0	408.0	404.0	
0.63	204.0	442.0	442.0	408.0	405.0	
1.35	504.0	789.0	799.0	754.0	745.0	
1.35	505.0	796.0	805.0	758.0	749.0	
1.35	505.0	797.0	806.0	758.0	750.0	
1.35	503.0	798.0	807.0	758.0	750.0	
1.65	507.0	875.0	879.0	826.0	817.0	
1.65	508.0	880.0	881.0	832.0	823.0	
1.94	511.0	896.0	895.0	891.0	893.0	
2.54	510.0	915.0	914.0	915.0	914.0	
2.54	510.0	914.0	914.0	914.0	913.0	
2.54	506.0	911.0	911.0	911.0	910.0	
2.86	506.0	990.0	917.0	918.0	917.0	Dryout No. 2, Saturation Temp 918°C
2.08	405.0	862.0	861.0	820.0	813.0	
2.38	411.0	871.0	870.0	862.0	867.0	
2.68	400.0	878.0	877.0	876.0	876.0	
2.99	400.0	980.0	885.0	885.0	885.0	Dryout No. 3, Saturation Temp 885°C
2.85	418.0	984.0	882.0	881.0	881.0	Dryout No. 3, Saturation Temp 885°C
2.73	395.0	961.0	878.0	878.0	877.0	Dryout No. 3, Saturation Temp 885°C
2.33	410.0	929.0	875.0	873.0	873.0	Dryout No. 3, Saturation Temp 885°C
2.33	399.0	873.0	872.0	864.0	869.0	
2.82	414.0	894.0	882.0	881.0	881.0	Dryout No. 4, Saturation Temp 882°C
2.99	398.0	962.0	884.0	884.0	883.0	Dryout No. 4, Saturation Temp 882°C
2.31	397.0	904.0	872.0	862.0	869.0	Dryout No. 4, Saturation Temp 882°C
2.31	404.0	874.0	873.0	862.0	866.0	
2.31	397.0	870.0	868.0	854.0	863.0	
1.79	604.0	911.0	912.0	909.0	910.0	
1.96	601.0	918.0	917.0	917.0	917.0	
2.14	610.0	926.0	926.0	926.0	926.0	
2.28	603.0	932.0	932.0	933.0	932.0	
2.51	603.0	929.0	939.0	941.0	939.0	
1.36	511.0	797.0	810.0	760.0	752.0	
1.36	501.0	793.0	807.0	757.0	748.0	Control Case